ACS SyntheticBiology

pubs.acs.org/synthbio

Research Article

Pattern Formation and Bistability in a Synthetic Intercellular Genetic Toggle

Bárbara de Freitas Magalhães,[⊥] Gaoyang Fan,[⊥] Eduardo Sontag, Krešimir Josić,* and Matthew R. Bennett*

Cite This: *ACS Synth. Biol.* 2024, 13, 2844−2860

Read Online

ACCESS | Metrics & More | Article Recommendations | Supporting Information

ABSTRACT: Differentiation within multicellular organisms is a complex process that helps to establish spatial patterning and tissue formation within the body. Often, the differentiation of cells is governed by morphogens and intercellular signaling molecules that guide the fate of each cell, frequently using toggle-like regulatory components. Synthetic biologists have long sought to recapitulate patterned differentiation with engineered cellular communities, and various methods for differentiating bacteria have been invented. Here, we couple a synthetic corepressive toggle switch with intercellular signaling pathways to create a "quorum-sensing toggle". We show that this circuit not only exhibits population-wide bistability in a well-mixed liquid environment but also generates patterns of differentiation in colonies grown on agar containing an externally supplied morphogen. If coupled to other metabolic processes, circuits such as the one described here would allow for the engineering of spatially patterned, differentiated bacteria for use in biomaterials and bioelectronics.

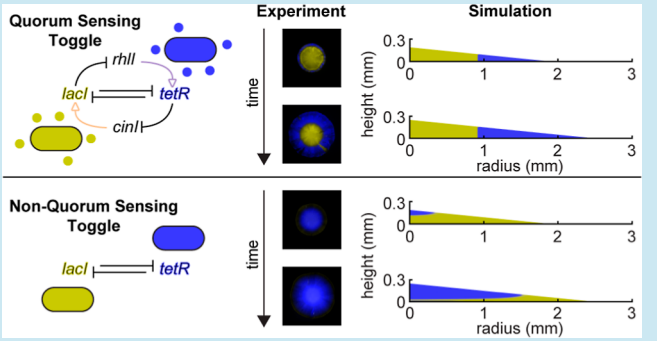

KEYWORDS: *genetic toggle switch, quorum sensing, pattern formation, self-organization, synthetic biology*

1. INTRODUCTION

One goal of synthetic biology is the creation of engineered biological systems that can perform a wide variety of functions.[1−4] Such systems could be used for various environmental, industrial, and medical applications.[5−8] Synthetic biology is also advancing basic research by providing a bottom-up approach to understand phenomena governed by nontrivial genetic regulatory mechanisms. This is done by creating and perturbing "synthetic gene circuits" in living systems that behave similarly to their natural counterparts and can thus serve as model systems.[9,10]

As part of the ground up approach to basic research, synthetic biologists have long sought to use engineered cells to recapitulate spatial patterns seen in multicellular systems.[9,11−15] Many mechanisms have been proposed to explain the appearance of natural patterning, such as the reaction−diffusion model[16] and the positional information model (or French flag model).[17] These mechanisms have been used as blueprints for synthetic analogues of biological patterns.[15,18,19] Scientists are also working toward self-organizing patterns[11,14,20−24] that use intercellular signals to regulate transcriptional activity.[20−23]

Indeed, the circuit topology of the first synthetic gene circuit to be described, the "genetic toggle switch",[25] has also been implicated in spatial patterning. The toggle switch comprises just two repressors that regulate each other's promoters, and it therefore has two possible transcriptional states corresponding to one active repressor gene, and the other repressed. Gene networks akin to the toggle switch are thought to help stabilize and refine spatial boundaries within differentiated populations because the two expression states of the toggle are generally mutually exclusive.[26] Toggle-like regulatory components are found throughout developmental processes, such as in the anterior-posterior development of the *Drosophila* blastoderm,[27,28] and in the dorsal-ventral development of the vertebrate neural tube.[29,30] In the absence of external signals, such toggle switches can function independently with the bias of each cell and its internal stochastic dynamics determining the transcriptional states of the respective toggle switches. However, an external morphogen gradient can result in spatial organization of cell states dependent on the local concentration of the signal.

Here, we built a version of the genetic toggle switch in *Escherichia coli* that uses intercellular signaling to reinforce each transcriptional state. For instance, if a cell is in the "ON" state it produces an intercellular signal that upregulates the ON state in

Received: April 17, 2024
Revised: July 12, 2024
Accepted: August 5, 2024
Published: August 30, 2024

https://doi.org/10.1021/acssynbio.4c00272
ACS Synth. Biol. 2024, 13, 2844−2860

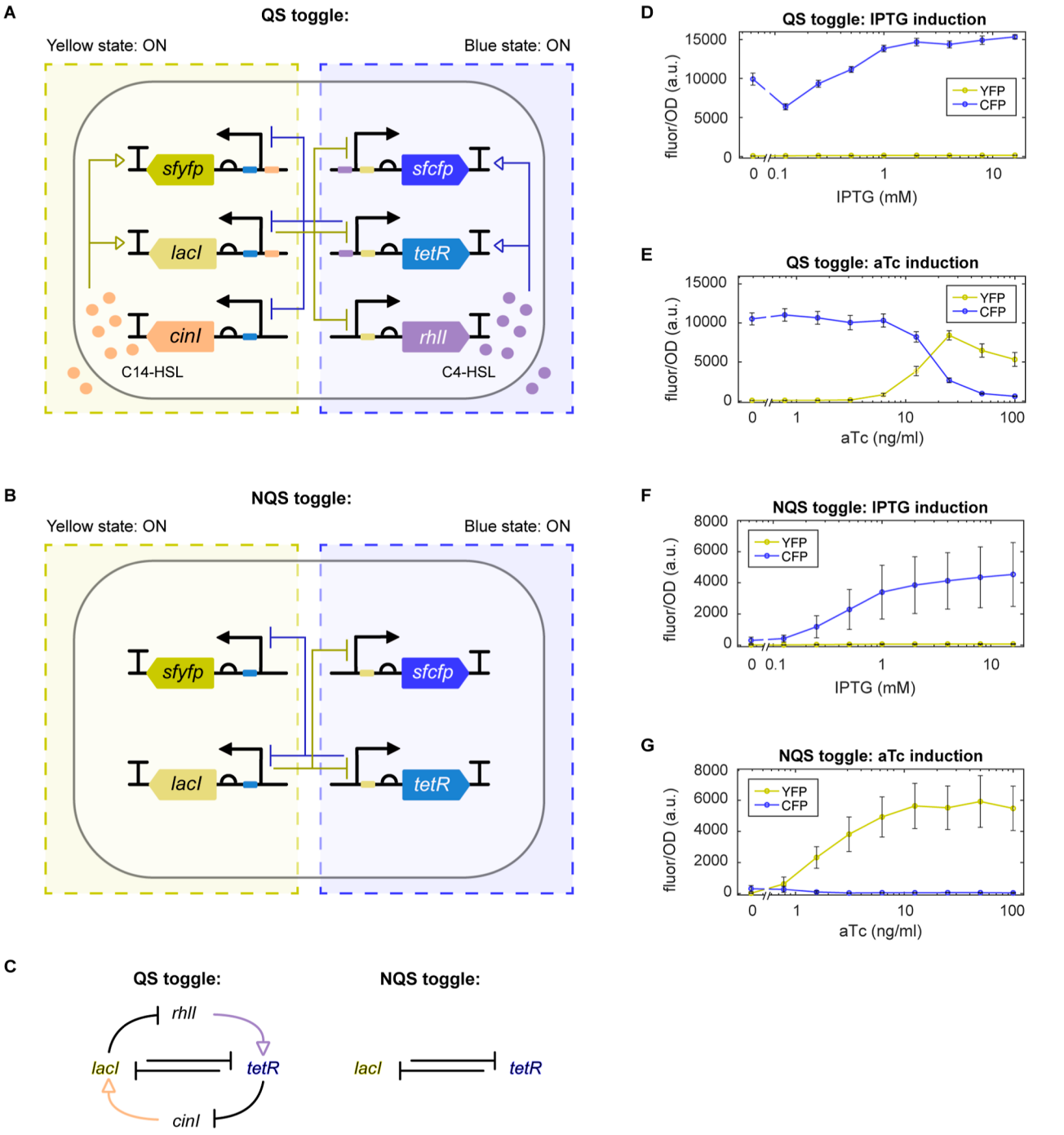

Figure 1. QS and NQS toggle circuit design. For both circuits, IPTG can induce the blue state, while aTc can induce the yellow. (A) QS toggle: when the yellow state is ON, LacI represses *tetR*, *rhlI*, and *sfcfp* genes, while C14-HSL activates *lacI* and *sfyfp* genes. When the blue state is ON, TetR represses *lacI*, *cinI*, and *sfyfp* genes, while C4-HSL activates *tetR* and *sfcfp* genes. (B) NQS toggle: when the yellow state is ON, LacI represses *tetR* and *sfcfp* genes. When the blue state is ON, TetR represses *lacI* and *sfyfp* genes. (C) The QS and NQS toggle topologies differ by the presence of two QS networks in the former. (D) QS toggle induction with IPTG in liquid culture. (E) QS toggle induction with aTc in liquid culture. (F) NQS toggle induction with IPTG in liquid culture. (G) NQS toggle induction with aTc in liquid culture. Lines represent the average fluorescence and error bars represent the standard deviation of three technical replicates for three independent experiments.

nearby cells. The addition of intercellular signaling to the toggle has been proposed as a means of creating a population-level toggle switch, allowing all cells in the population to simultaneously reside in one of the two possible transcriptional states.[31,32] We experimentally confirm that given the right conditions this version of the toggle does exhibit population-level bistability in a well-mixed liquid culture. Additionally, we show that when grown on solid agar imbued with an exogenous morphogen, colonies of these cells form three-dimensional patterns that differ from those observed in colonies of cells containing a traditional toggle switch lacking intercellular signaling. In particular, the addition of intercellular signaling creates a regime in which cells in the center of the colony stay ON, while in the absence of such signaling, the center of the colony turns OFF. The insertion of morphogen-coupled intercellular signaling can potentially prolong the state

https://doi.org/10.1021/acssynbio.4c00272
ACS Synth. Biol. 2024, 13, 2844−2860

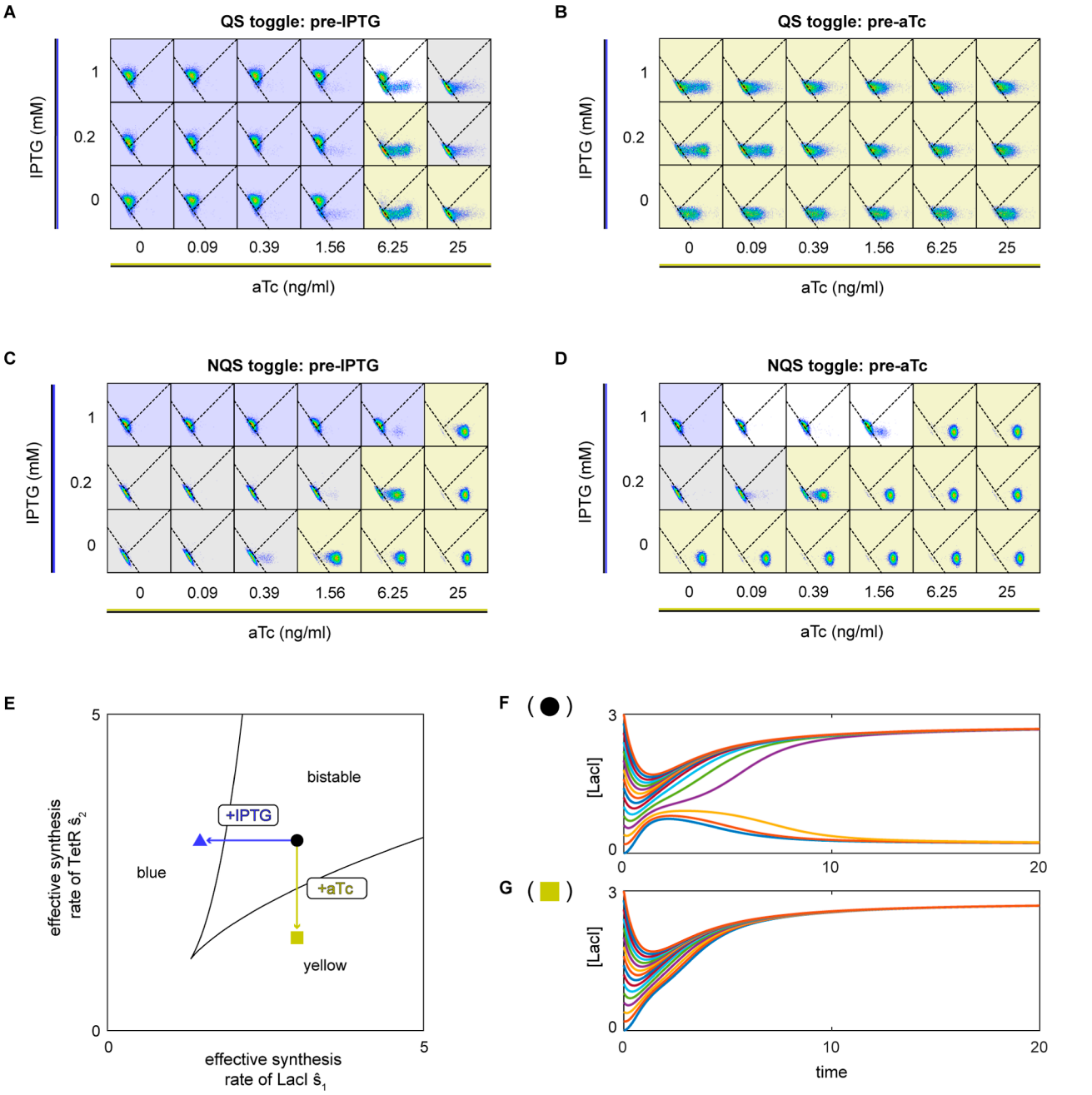

Figure 2. Behavior of QS and NQS toggle cells when treated with a combination of inducers. (A,B) Flow cytometry data of QS toggle cells that were preinduced with either IPTG (A) or aTc (B). Each dot is a single cell classified within a gate. Gates were determined with single color and double negative controls. Dashed lines in each plot represent the boundaries between the three distinct gates, which represent cellular states: CFP+ (top gate), YFP+ (bottom-right gate), and OFF (bottom-left gate). Background colors in each plot represent which state the majority of cells are in (>50%): blue plots indicate mostly CFP+ cells, yellow plots are mostly YFP+, gray plots are mostly OFF, and white plots indicate cells that are present in multiple states (<50% each). (C,D) Flow cytometry data of NQS toggle cells that were preinduced with either IPTG (C) or aTc (D). (E) Bifurcation diagram of the QS toggle system with nondimensionalized parameters $\hat{s}_1$ and $\hat{s}_2$, representing the effective synthesis rate of repressors (eq 3). Here, without exogenous inducers, aTc or IPTG, the system is bistable (black dot). Adding aTc or IPTG (blue triangle and yellow square respectively), lowers the corresponding effective synthesis rate of repressors, which in turn results in a monostable system. (F,G) Sample trajectories of the QS toggle model with different initial conditions for parameters marked by the black dot and yellow square in (E). Variables and parameters in (E−G) are nondimensionalized (see Methods).

determined by the morphogens. Thus, intercellular signaling can be an important factor in extending cellular memory and coordinating a population. We develop a mechanistic mathematical model of the system to explain how degradation, diffusion, and sequestration of external inducers coupled with colony expansion determine the observed patterns.

2. RESULTS AND DISCUSSION

2.1. General Characteristics of QS and NQS Toggles.

We first built a version of the genetic toggle switch with intercellular signaling to test whether it creates a population-level behavior that differs from a conventional toggle population. We call this version of the toggle switch that includes

https://doi.org/10.1021/acssynbio.4c00272
ACS Synth. Biol. 2024, 13, 2844−2860

intercellular signaling the "QS toggle", as it uses refactored quorum sensing pathways to generate intercellular signals. The QS toggle is a version of the genetic toggle switch[25] that includes two repressors that repress each other's promoters (LacI and TetR). Additionally, it includes a reporter for each state (YFP and CFP) and two orthogonal QS pathways (CinR/I and RhlR/I)[33−35] to produce the necessary intercellular signaling. A representation of the QS toggle's two fluorescent states is shown in Figure 1A. For the yellow state to be active (Figure 1A, left), LacI represses the promoters driving the expression of *tetR*, *cfp*, and *rhlI*. With *tetR* repressed, *cinI* is expressed, and its protein catalyzes the production of C14-HSL. When bound to the CinR transcription factor, C14-HSL activates the expression of *lacI* and *yfp*. Alternatively, for the blue state to be active (Figure 1A, right), TetR represses the promoters driving the expression of *lacI*, *yfp*, and *cinI*. With *lacI* repressed, *rhlI* is expressed, and its protein produces C4-HSL. When bound to the RhlR transcription factor, C4-HSL activates the expression of *tetR* and *cfp*. One can exogenously induce the yellow state by adding anhydrotetracycline (aTc), which will inactivate TetR (Figure 1E). Similarly, one can exogenously induce the blue state by adding isopropyl-β-D-1-thiogalactopyranoside (IPTG), which activates LacI (Figure 1D). The QS toggle is unbalanced in the absence of inducers: it exhibited a preference for the blue state (Figure 1D,E). We also found that this imbalance is dependent on the QS network (Figure S1I,J). A comparison of the regulatory architectures of the QS toggle and the traditional non-quorum sensing toggle (or "NQS toggle") is shown in Figure 1C. The QS toggle topology (Figure 1C, left) differs from the NQS toggle (Figure 1C, right) topology by the presence of two QS networks, creating extra positive feedback loops. The NQS circuit includes the same repressors and reporter genes but is driven by promoters that responded only to the respective repressors (Figure 1B). The NQS toggle can also be tuned with IPTG and aTc (Figure 1F,G). For all experiments, we transformed the plasmid-borne QS and NQS circuits into an *E. coli* strain (CY027, see Methods) that contains constitutively expressed *cinR* and *rhlR* in its genome.

We first checked whether cells containing the QS toggle exhibited population-level bistability. Genetic toggles are often bistable,[25,36−38] i.e., they can stably reside in either of two possible transcriptional states. To find the bistable region for both the QS and NQS toggles, we grew overnight cultures with either IPTG or aTc to allow for the populations to start in either state (blue or yellow, respectively). We then grew these cells in liquid culture using various combinations of IPTG and aTc concentrations and used flow cytometry to measure the CFP and YFP fluorescence of individual cells. After 3 h, we observed that, when starting in the yellow state (i.e., previously grown in media with aTc), QS toggle cells all remained in the yellow state for all combinations of inducer tested (Figure 2A, right). However, when starting in the blue state (i.e., previously grown in media with IPTG), QS toggle populations shifted to the yellow state at sufficiently high aTc concentrations but remained in the blue state at lower concentrations (Figure 2A, left). Importantly, we observed cultures in which all cells were either in the blue or yellow state depending on the starting condition and the inducer concentration (Figure 2A), indicating that the QS toggle is bistable at the population level in those conditions. Meanwhile, NQS toggle cells transitioned to blue and yellow when starting from the opposite color initial conditions (Figure 2B). We also observed that cells preinduced with IPTG primarily did not show any fluorescence (Figure 2B, left), although the blue state was inducible. A third state (OFF), in which cells exhibited little to no fluorescence of either type, was more common within NQS cells. The NQS toggle was also bistable for some conditions. When we grew the cells for 9 h instead of 3, the NQS toggle showed a decrease in both intensities in all tested conditions, while the QS toggle tended to show stronger fluorescence intensities (Figure S2).

We next developed a mathematical model and identified the parameters that determine whether the QS toggle switch is bistable. Denoting by $x(t)$ and $y(t)$ the concentrations of LacI and TetR, respectively, and by $g(t)$ and $h(t)$ the intracellular concentrations of QS signals, C14-HSL, and C4-HSL, respectively, the model takes the form

$$\dot{x} = a_1\eta_1(y)\phi_1(g) - (\gamma_1 + \gamma_d)x \tag{1a}$$

$$\dot{y} = a_2\eta_2(x)\phi_2(h) - (\gamma_2 + \gamma_d)x \tag{1b}$$

where the parameter a_i determines the maximal production rates, γ_i is the degradation rates for LacI and TetR (numbered i = 1 and 2, respectively), and γ_d is the rate of dilution due to cell growth. We model the repression and activation of the promoters using Hill functions η_i and ϕ_i, respectively. The intracellular concentration of QS signals obeys similar equations (see Methods for the full model).

We nondimensionalized eq 1a and performed a bifurcation analysis (see Methods) to confirm the existence of a region of bistability in the parameter space of the QS toggle system model. The behavior of the toggle switch is driven by the QS signals present in each cell. The dynamics of the QS signals are, in turn, determined by the rate at which they are produced and degraded, with the degradation rate being significantly slower than its production and LacI/TetR dynamics. Because degradation is slow, we will analyze the behavior of the toggle both at intermediate time scales, when the degradation and production are not balanced, and at long time scales, when the QS signal concentration reaches equilibrium. Let $\hat{g}(t)$ and $\hat{h}(t)$ represent the normalized QS signal concentration at time t. In the absence of inducers, the behavior of the system is determined by the effective synthesis rate of repressors (see Methods for the derivation)

$$s_1(t) = \frac{a_1}{(\gamma_1 + \gamma_d)\theta_1}\frac{\hat{g}(t)}{1 + \hat{g}(t)}, \qquad s_2(t) = \frac{a_2}{(\gamma_2 + \gamma_d)\theta_2}\frac{\hat{h}(t)}{1 + \hat{h}(t)} \tag{2}$$

Here, θ_x and θ_y are the thresholds for LacI and TetR repression, respectively, used in the Hill functions, η_i. As exogenous inducers, IPTG or aTc, are added to the system, derepression decreases the effective synthesis rate of the repressors. It follows that the new effective synthesis rate of repressors is (see Methods for details)

$$\hat{s}_1(t) = \frac{s_1(t)}{1 + \hat{v}_0}, \qquad \hat{s}_2(t) = \frac{s_2(t)}{1 + \hat{u}_0} \tag{3}$$

where $\hat{v}_0$ and $\hat{u}_0$ denote the normalized IPTG and aTc concentrations, respectively. An example of the effect of induction with aTc, and the resulting derepression of TetR, is shown in Figure 2E−G: Induction leads to a drop in the bifurcation parameters, $(\hat{s}_1, \hat{s}_2)$, driving the system out of the bistable region of parameters state to the yellow, monostable state.

https://doi.org/10.1021/acssynbio.4c00272
ACS Synth. Biol. 2024, 13, 2844−2860

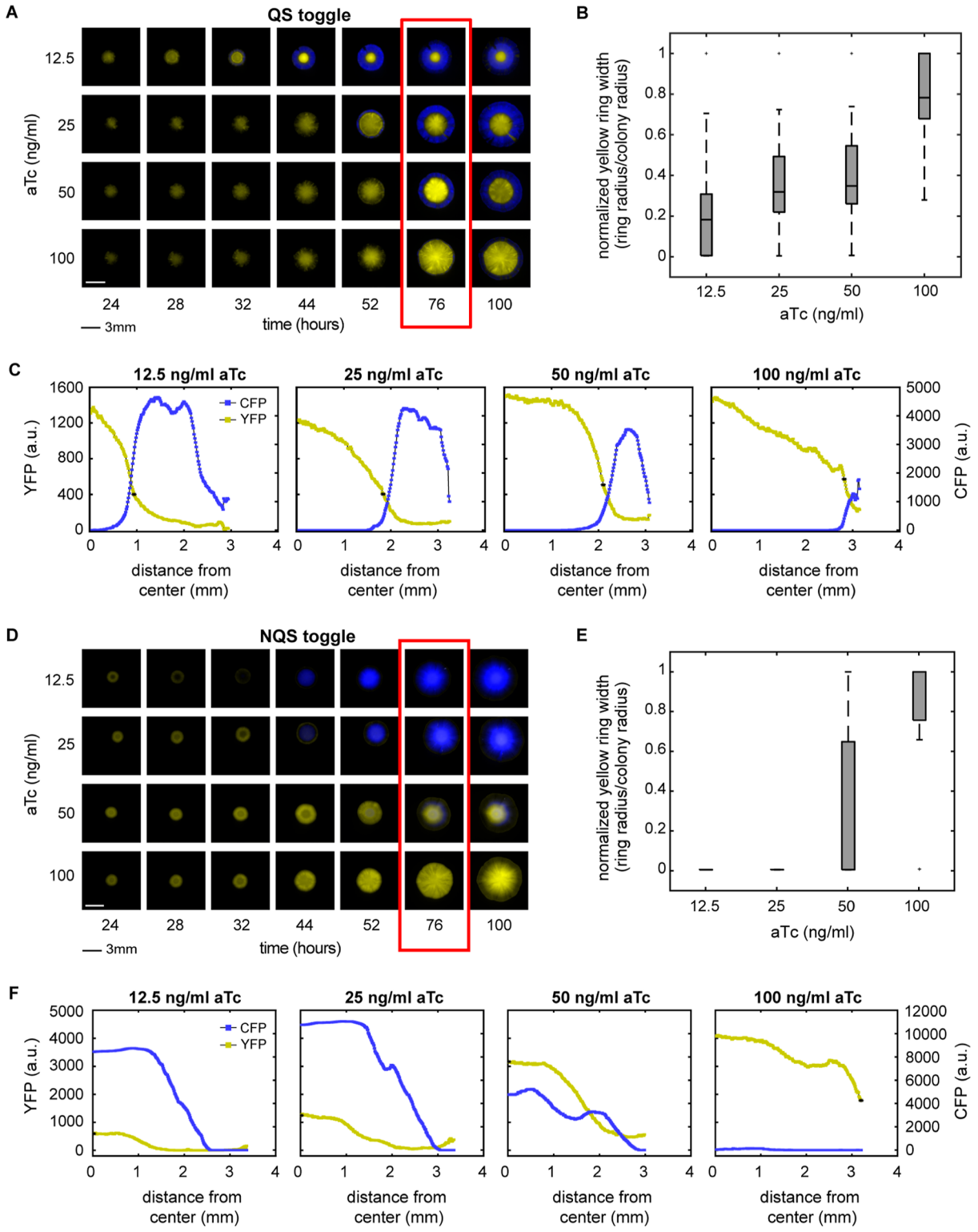

Figure 3. Expanding QS and NQS toggle colonies show aTc-dependent patterning. (A) QS toggle colonies obtained from plates with different initial aTc concentrations, shown at different times. (B) Yellow ring width (center disc) was measured among all colonies to quantify the pattern. The width was determined as the distance from the center to the threshold point, at which yellow fluorescence fell below 30% of its maximum. The only pairwise combination of widths not found to be statistically different was 25 and 50 ng/mL aTc ($p < 0.01$, Kruskal–Wallis nonparametric test). Data represent at least 11 independent experiments. (C) Fluorescence intensity cross-sectionals of the colonies shown in red in (A). Curves represent the average fluorescence of 4 radii (90° apart) of the same colony. (D) NQS toggle colonies obtained from plates with different initial aTc concentrations, shown at different times. (E) Yellow ring width was used to quantify the patterns as in (B). We considered yellow ring width to be zero when blue cells dominate the center (see Methods for a full set of assumptions). All pairwise combinations that included 100 ng/mL aTc were found to be statistically different (*$p < 0.01$, Kruskal–Wallis nonparametric test). Data represent two independent experiments. (F) Fluorescence intensity cross-sectionals of colonies shown in red in (C). Curves represent the average fluorescence of 4 radii (90° apart) of the same colony.

https://doi.org/10.1021/acssynbio.4c00272
ACS Synth. Biol. 2024, 13, 2844−2860

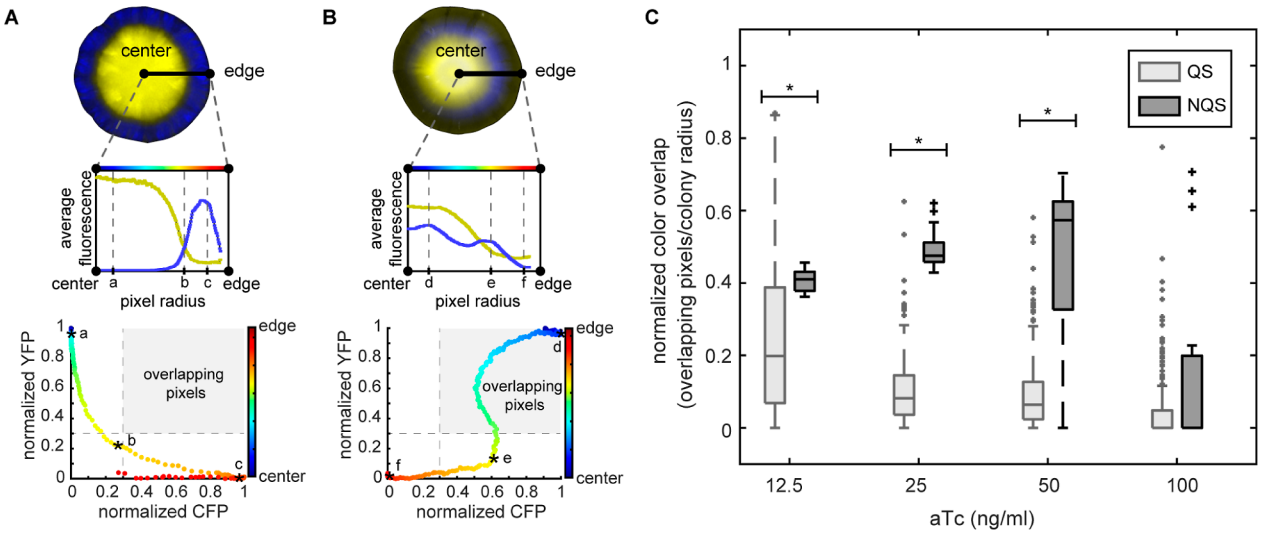

Figure 4. QS colonies create better radially separated patterns than NQS colonies. Measurement of color overlap was used to quantify the spatial segregation of states in each colony. Average fluorescence of each colony's radii plotted from the center of the colony to the edge (A,B, top plots). Each pixel was also plotted for both normalized fluorescence values (A,B, bottom dot plots). Pixels were classified as overlapping when both normalized fluorescence values were above a predefined threshold (inside the gray boxed region). (A) Example of a behavior of QS colonies. The QS colony shown is the same as that in Figure 3A, at 50 ng/mL and 76 h. Asterisks (a−c) show the same pixels in both plots. (B) Example of a behavior in NQS colonies. The NQS colony shown is from Figure 5C, 50 ng/mL at 76 h. Asterisks (d−f) show the same pixels in both plots. (C) Quantification of pixel overlap for QS (light gray) and NQS (dark gray) colonies. The number of overlapping pixels was normalized by the colony radius (total). *$p < 0.01$, Mann−Whitney nonparametric test. Data for each QS test contain over 180 colonies from at least 11 independent experiments, while data for each NQS test contain at least 15 colonies from 2 independent experiments.

The mathematical model thus predicted that bistability depends on the QS network and relative effective synthesis rate of the repressors. We tested this prediction experimentally by engineering a few variants of the QS toggle that changed those factors (see the Supporting Information). These variants exhibited changes in state preference, agreeing with the prediction of the model (Figure S1).

2.2. QS and NQS Toggle Behavior in Colonies. We next asked how the QS toggle behaves in an environment in which the signals are not homogeneously distributed in the population, allowing spatial patterns to arise. To do this, we grew QS and NQS toggle colonies in LB agar plates containing aTc and monitored their growth and fluorescence over time.

Most strikingly, we noticed that many QS toggle colonies formed a blue ring surrounding a yellow disc (Figure 3A), with the size of the yellow disc correlated to the aTc concentration in the agar (Figure 3B). ATc is known to be temperature sensitive.[39] Since aTc induces the expression of the yellow state, we hypothesized that thermally induced aTc degradation was driving the emergence of blue cells. Indeed, we verified that the preincubation of aTc plates at 37 °C directly (before cells are plated) alters the blue ring size and time of appearance (Figure S3). Thus, the decay of aTc creates a temporal morphogen gradient, resulting in a switch in the state of some of the population.

In the images of QS toggle colonies, we observed little overlap between cells in the yellow and blue states (Figure 3C). Over time, the blue ring generally expanded as the colony grew, but the boundary between the yellow and blue cells remained roughly fixed. Wherever cells in the blue state took over, the yellow fluorescence tended to decrease.

When grown on solid media, the NQS toggle behaved differently from the QS toggle. Like the QS toggle, NQS toggle colonies were initially yellow when the media contained a sufficiently high concentration of aTc. Cells in the blue state emerged eventually but did so in a way distinct from what we observed in the QS toggle: blue cells first appeared in colony centers, and did so earlier and at lower aTc concentrations (Figure 3D). Most NQS toggle colonies grown with 12.5−50 ng/mL aTc showed blue cells in the center at 76 h (Figure 3E), which resulted in yellow region width measurements close to zero (see Methods).

One of the main differences in the spatial patterns between the two toggles was the degree of radial separation between the states. The QS toggle colonies appeared to segregate well in contrast to the NQS toggle colonies (Figure 3F). To quantify the level of segregation, we measured the pixel color overlap in images from both QS and NQS colonies: For each pixel, we measured the intensity of both blue and yellow fluorescence, and in Figure 4A,B (bottom panels), we show the normalized YFP and CFP fluorescence as a function of distance from the center of the colony. We said that colors overlapped in a pixel when the values of both YFP and CFP fluorescence intensities were each above a threshold of 0.3 (out of a maximum intensity normalized to 1). To obtain the relative overlap count for a colony, we divided the number of overlapping pixels by the total number of pixels covering the colony radius (Figure 4C).

Color overlap was significantly higher in the NQS compared to QS colonies in 12.5, 25, and 50 ng/mL aTc plates ($p < 0.01$, Mann−Whitney nonparametric test). In 100 ng/mL aTc plates, we observed little overlap with both circuits, mostly because not all colonies contained cells in the blue state. When we excluded from analysis colonies with cells in only one state, NQS colonies displayed higher overlap than QS colonies at all aTc concentrations (Figure S4).

A smaller overlap of colors in the image indicates a better spatial separation between cells in the two corresponding states along the radial direction of a colony. Therefore, QS cells in different states were better segregated radially than NQS cells. Since we imaged the colony from above, the higher degree of

https://doi.org/10.1021/acssynbio.4c00272
ACS Synth. Biol. 2024, 13, 2844−2860

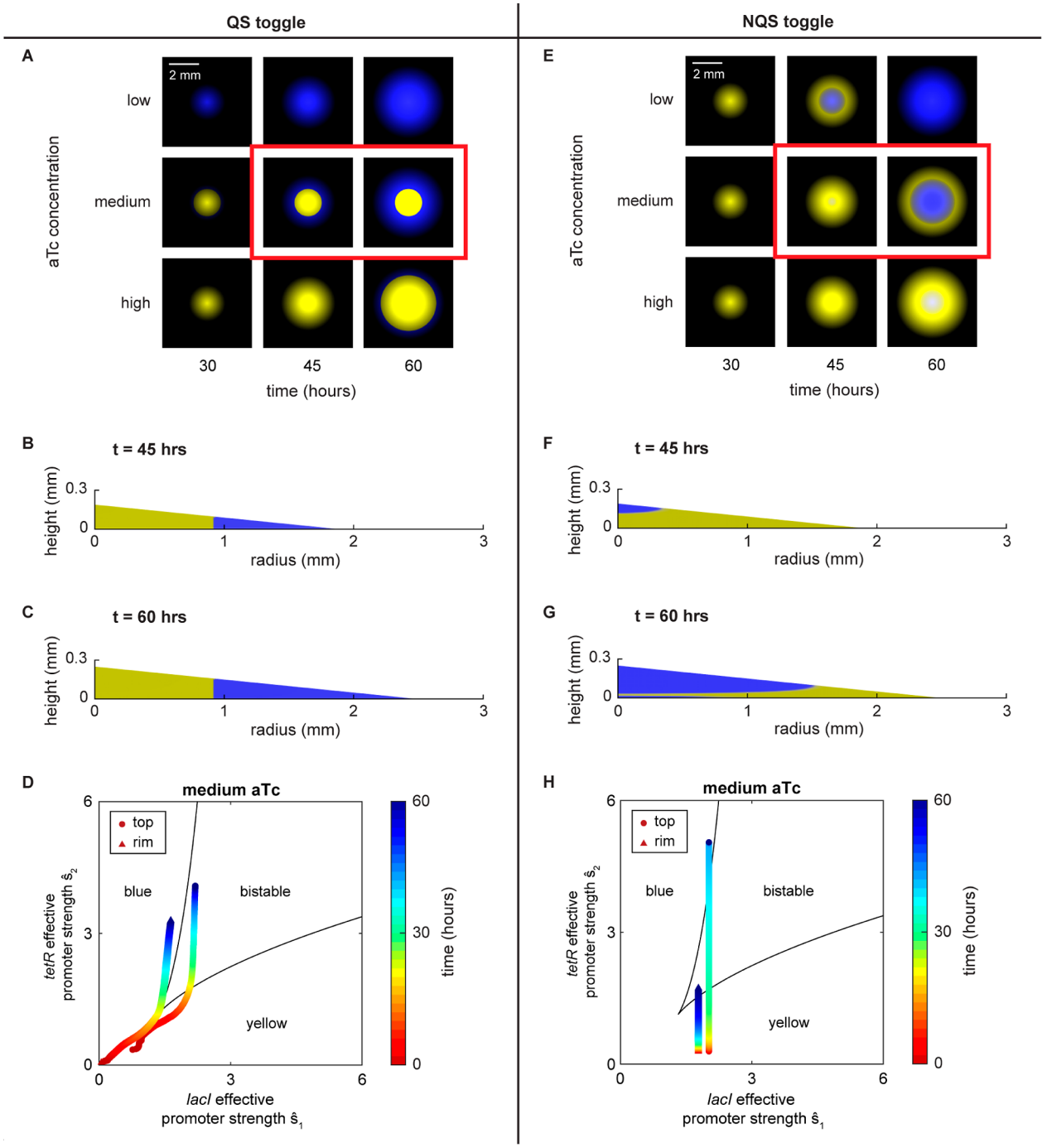

Figure 5. Mathematical model simulations of QS and NQS toggles. (A) Simulations of the QS colony show that a blue outer ring emerges. The time at which the ring emerges, and its size depend on initial aTc concentration. (B,C) The cross-sectional view of the model colonies shows that the cells in the two states are radially segregated. The boundary between the two states is roughly fixed, in agreement with experiments. (D) Trajectories of the effective synthesis rate of repressors through the bifurcation diagram for cells at the top (circle) and rim (triangle) of the QS colony. (E) Simulations of the NQS colony at different times and initial aTc concentration show the emergence of cells in the blue cells at the center of the colony. (F−G) Cross-sectional view of the model colonies at different times. Cells enter the blue state first at the top of the colony and the blue wave travels downward. Cells in the two states remain vertically segregated. (H) Bifurcation diagram showing the bifurcation parameters' trajectories of cells at the top (circle) and rim (triangle) of the NQS colony.

overlap in the NQS case could indicate either that cells in the two states are intermingled or that they are segregated vertically. To test which of these hypotheses is more likely, we extended our mathematical models of both the QS and NQS systems to include spatial effects, such as colony expansion and the diffusion of inducers (and intercellular signaling molecules when pertinent) within the agar and the colony. We assumed that the colony is conical and grows through the addition of cells in an active growing zone at the interface of the colony with agar[40] (see Methods).

Simulations of our expanded models recapitulated experimental observations and suggested answers to our questions about the observed segregation of cells in different states. In the simulated QS toggle colony (Movie S1), when the colony is

https://doi.org/10.1021/acssynbio.4c00272
ACS Synth. Biol. 2024, 13, 2844−2860

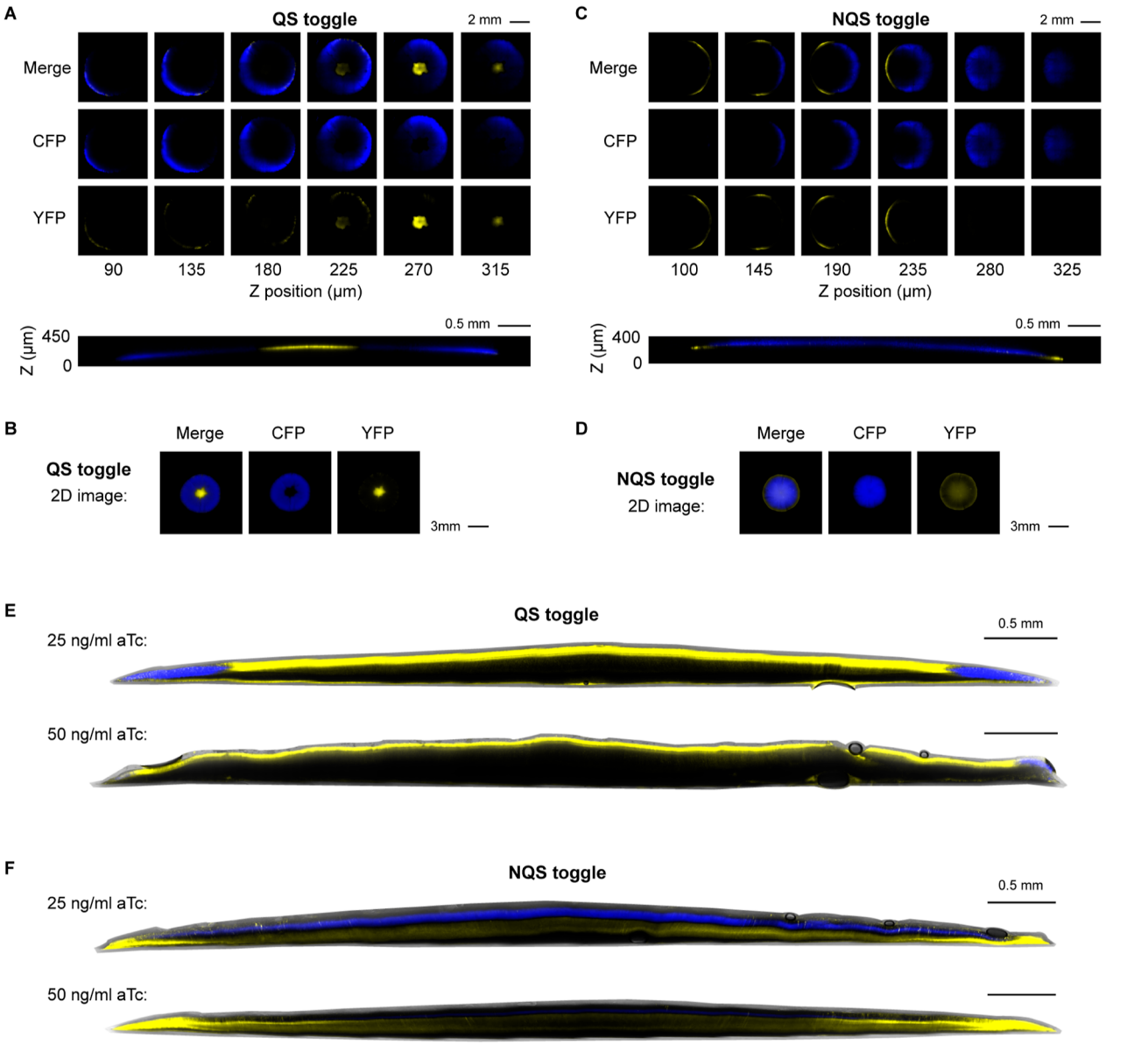

Figure 6. Three-dimensional view of QS and NQS colonies. (A) QS toggle layers from bottom to top of colony (left to right). Orthogonal view of the QS toggle frames is shown below. Colony is not more than 250 μm tall. (B) 2D image of the same colony in (A) for comparison. Separate fluorescence channels are shown. (C) NQS toggle layers from bottom to top of colony (left to right). Orthogonal view of the NQS toggle frames is shown below. (D) 2D image of the same colony in (C) for comparison. Separate fluorescence channels are shown. (E) Slices of different QS colonies grown in either 25 or 50 ng/mL aTc. (F) Slices of different NQS colonies grown in either 25 or 50 ng/mL aTc.

small, abundant aTc and basal C14-HSL production led to the establishment of the initial yellow state across the colony. This state was then reinforced by the accumulated C14-HSL signal. Equation 2 shows that dilution due to growth effectively lowers the synthesis rate of repressors s_1 and s_2. The differential effect of growth consequently results in distinct behaviors of cells growing at different rates. We examined the state of several regions of the colony by tracking the bifurcation parameters, ($\hat{s}_1$, $\hat{s}_2$), from eq 3, at the center (top) and the periphery (rim) of the QS colony over time (Figure 5D). Cells that are not growing or growing slowly, such as those at the top of the colony, stayed in the bistable region and remained yellow. This explains the experimental observation that the center of the colony remains yellow, despite reduced aTc levels due to degradation (at a 37 °C incubation temperature). In contrast, for the fastest-growing cells at the periphery, the drop in aTc concentration and the slow accumulation of the C4-HSL signal from basal production allow cells to enter the monostable blue state (Figure 5B). Newborn cells at the bottom of the colony are in the same state as their parent cells. Together, this explains why in the QS toggle color overlap is small (vertical slices are in the same state), and the boundary between the yellow and blue states is maintained at the point where the first cells turn blue (Figure 5B,C), in agreement with experimental observations (Figure 3A). Simulations also show that higher aTc concentrations lead to the outer rings of blue cells emerging later in time (Figure 5A).

In the simulations of the NQS toggle colony (Movie S2), with the initial smaller colony sizes and abundant aTc supply from the agar, aTc levels are relatively high everywhere in the colony. This explains the initial colony-wide yellow state we observed in the experiments (Figure 3D). The top of the colony is further from the aTc source (agar), so that a top-down aTc gradient forms

https://doi.org/10.1021/acssynbio.4c00272
ACS Synth. Biol. 2024, 13, 2844−2860

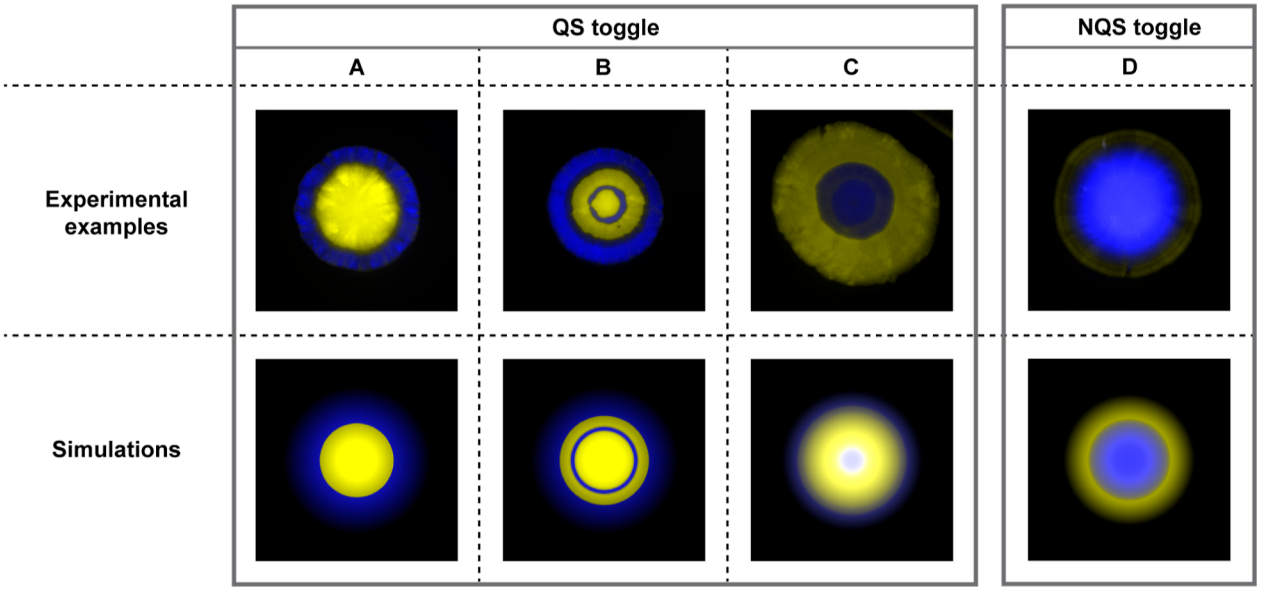

Figure 7. Four types of patterns obtained from experiments (top) and mathematical simulations (bottom). (A) QS toggle colony pattern, with radial segregation of states and blue emergence at the edge of the colony, forming an external blue ring. (B) Alternative QS toggle pattern, with radial segregation of states and multiple blue rings (internal and external). (C) Inverted QS toggle pattern, where radial segregation of states and blue emergence at the center occur only in specific conditions (see the Supporting Information). (D) NQS toggle colony pattern, with vertical segregation of states and blue emergence at the center of the colony.

over time. As the colony grows, the aTc level at the top, where concentration is lowest, eventually degrades below the point needed to keep cells in the yellow state, causing the top of the colony to turn blue. Cells entering the blue state produce TetR, which enables aTc sequestration, further lowering surrounding aTc levels. As a result, we observed a blue wave traveling downward from the top of the colony (Movie S2). For the growing cells at the periphery, cells stay yellow despite the dilution effect, which is consistent with the observation that aTc concentration needs to be low to cause a switch in state for a fast-growing liquid culture (Figure 1G). In Figure 5H, we track the effective synthesis rate of repressors for cells at the center (top) and the periphery (rim) of the NQS colony over time. In simulations, the state of the top of the colony moves from the bistable region to the monostable blue region, while the rim of the colony remains yellow (Figure 5F,G). Thus, our model predicted that the two states are vertically segregated in NQS colonies, suggesting that spatial segregation rather than heterogeneity is responsible for the experimentally observed color overlap. Our simulations and bifurcation analysis also revealed that at higher initial aTc concentrations, the blue state takes over from the top at a later time (Figure 5E), as it takes longer for aTc to degrade to the hysteresis point at which cells can switch states.

To test the predictions of the model about the different spatial structures in the QS and NQS colonies, we used confocal microscopy to image the 3D structures of the colonies (Figure 6). We also sliced the colonies vertically and imaged their cross sections using confocal microscopy (see Methods). For the QS toggle, 3D confocal images of QS toggle colonies displayed radial separation between the states, confirming the predictions of the model and in agreement with our earlier analysis of experimental findings (Figure 6A,E). Depending on the aTc concentration, the QS toggle cells at the top of the colony remained yellow, and blue cells only appeared in the outer part of the colony. Imaging of the colony slices also confirmed this observation (Figure 6E). In contrast, we observed that the NQS colonies showed vertical segregation, with cells at the top of the colony dome in the blue state and cells at the bottom in the yellow state (Figure 6C,F). The slices confirmed that cells in the blue state occupied the top of the NQS colonies, while cells in the yellow state occupied the bottom, as predicted by the model (Figure 6F).

We found that ring formation in the QS toggle exhibited some variability and randomness, causing imperfect radial symmetry of the outer blue rings. Despite this variability, the difference in color segregation between QS and NQS colonies was statistically significant (see Figure 4). Occasionally, we also observed the occurrence of multiple blue rings, i.e., the formation of internal and external blue rings in QS toggle colonies (Figures 7 and S5). In addition, patches of blue cells sometimes failed to form a full ring (Figure S5). These observations suggested that external or internal fluctuations could play a role in determining the observed spatial patterns. Noise can cause jumps between the stable states of a bistable system. However, we expect such switches to be localized in the absence of a mechanism that can synchronize the state across the entire colony at once. Thus, we concluded that external fluctuations that affect all or most of the colony were more likely to drive the emergence of complex spatial patterns, such as multiple rings. Furthermore, when the QS toggle was grown in a different medium (solid EZ rich defined medium instead of LB agar), the outer blue ring pattern was disrupted. At times, we observed blue cells emerging from the center of the colony at 100 ng/mL of aTc. These patterns resembled those in the NQS toggle in LB agar (Figures 7 and S6).

We were able to obtain similar patterns in numerical simulations by changing parameter values or by including extrinsic perturbations in the model we described above (Figure 7 and Methods). We found that a pulse of increased repressor degradation can result in the formation of multiple rings in the QS colony. Such pulses might be caused, for instance, by

https://doi.org/10.1021/acssynbio.4c00272
ACS Synth. Biol. 2024, 13, 2844−2860

transient extrinsic fluctuations in experimental conditions. Moreover, a persistent decrease in the synthesis rate of both repressors (perhaps caused by differences in the growth media) can lead to an inverted pattern (Figure 7C) in the QS system. Thus, the complex spatial patterns we observed in some experiments can be explained using the same mechanisms underlying the predominant, single ring patterns. The variability of multiring patterns, along with the high dimensionality of the model parameter space, makes it difficult to examine such patterns systematically. A full understanding of how these complex patterns emerge and how they can be controlled will thus require the development of new experimental approaches.

3. DISCUSSION

Patterns, and especially ring-like patterns, formed by synthetic gene circuits are not new. Previous studies have utilized various methods to create patterns, such as internal genetic oscillations,[41] scale-invariant intracellular signaling,[20] or mechanical interactions between cell types.[42] Here, we show that toggle switches can also create patterns in colonies based on how they shape the cells' responses to a morphogen. Specifically, the classical NQS toggle creates a vertically segregated pattern, while the QS toggle leads to a segregated ring structure. We also developed a mathematical model that captured both behaviors. An analysis of the model suggests that, in the NQS case, the sequestration of signals and geometry of the colony lead to the formation of a morphogen gradient inside the colony, creating top-down segregation. In contrast, the model suggests that faster cell growth at the periphery of QS toggle colonies and the QS signal gradient inside the colonies lead to the emergence of an outer blue ring. The difference is that as the aTc level decreases in the QS toggle, signaling between cells in the yellow core helps to lock them in the same state. However, in the NQS toggle, the blue state becomes monostable in the absence of aTc and signals from other cells. As the aTc concentration is lowest at the top of the colony, a wave of transitions from the yellow to the blue state propagates from the colony's top downward. Our mathematical analysis implies that bistability is determined by the external morphogen concentration and the effective synthesis rate for each repressor, which is, in turn, determined by protein production, proteolytic degradation, dilution, and QS signals.

Our mathematical model provided further insights into the mechanisms behind the formation of patterns. When pattern formation is modeled on the time scale of hours, one must account for expanding colony size. As suggested by Warren et al.,[40] an actively growing layer at the bottom of the colony drives the "establishment phase" (14−24 h). After 24 h, the colony enters a "flattening phase", during which vertical growth slows while radial growth remains linear. In our model, the characteristic length scale of signal diffusion is much larger than the size of a colony, and thus, details of the colony expansion mechanisms do not have a large impact. We thus assumed that model colonies grow linearly in both the vertical and radial directions. The location of newly born cells, on the other hand, does matter. As new cells inherit the state of their parental cells, where the effective synthesis rate of repressors of the newly born cells land in the bistable region determines the emergent patterns in the colony.

It should be noted that our model does not precisely predict the full behavior of the colonies. Our experiments showed that fluorescence intensities were lower in the bulk of many colonies and higher nearer the surface (Figure 6E). This indicates that the colonies are more complex than our model suggests. Yet, our model still provides qualitative insights into the formation of the patterns and their symmetries. Further experimental studies on *E. coli* colony growth, structure, and metabolism, especially at larger colony sizes, will allow for the improvement of the mathematical model and a better understanding of pattern formation in microbial colonies.

Our work indicates that the observed spatial patterns are dependent not just on the underlying genetic circuitry but also on growth conditions and cellular metabolism. Our mathematical model allows us to identify which patterns are allowed by the system and the mechanisms that generate them. The presence or absence of intercellular communication, for instance, is not a determinant of a single pattern. Rather, the resultant pattern is determined by multiple factors, including morphogen concentration, the synthesis rate of repressors, and intercellular signaling. Nevertheless, the presence of intercellular signaling allows one to actively control or shape the balance by implementing more spatial features, such as signal degradation by differentiated cells or external flux. These patterns shed light into how synthetic multicellularity can be created in bacteria and provide a further step toward the creation of large-scale, programmable synthetic multicellular systems.

4. METHODS

4.1. Plasmids and Strains. We constructed plasmids with either PCR-based, restriction enzyme cloning, or Golden gate assembly methods. QS and NQS toggles, as well as all other tested versions, are composed with three plasmids each, providing resistance to kanamycin, chloramphenicol, and spectinomycin. A list of all plasmids employed is provided in Table S1. For this study, we used the CY027 *E. coli* strain, a BW25113 derivative.[43] This strain has the *lacI*, *araC*, and *sdiA* genes knocked out, and constitutive *cinR* and *rhlR* knocked-in to its genome to enable QS communication (Δ*lacI*, Δ*araC*, Δ*sdiA*, *Ptrc*-cinR*, and *Ptrc*-rhlR*).

4.2. Plate Reader Experiments. From single colonies, we inoculated cells containing the appropriate plasmids into 5 mL of LB with antibiotics (50 μg/mL kanamycin, 34 μg/mL chloramphenicol, and 50 μg/mL spectinomycin) for overnight growth at 37 °C in a shaker (250 rpm). Then, we diluted the culture 1:100 in minimal M9CA broth (Teknova) with antibiotics, and we grew these cells for 2 h in a 37 °C shaker (250 rpm). Meanwhile, we prepared 96-well round-bottom plates with minimal M9CA broth, antibiotics, and applicable inducers (IPTG and aTc) with a twofold final concentration of 100 μL per well. After the 2 h growth, we added 100 μL of cell outgrowth to each well (1:1). We incubated the plates at 37 °C and shaking at 800 rpm. After 2 h, we read each plate in a Tecan Infinite M1000 for growth (OD, 600 nm), YFP fluorescence (ex, 514 nm; em, 527 nm), and CFP fluorescence (ex, 433 nm; em, 475 nm). We used cells without plasmids to measure background autofluorescence. The results shown are reported as (fluorescence-background)/OD_{600}.

4.3. Flow Cytometry. We inoculated cells from single colonies into 5 mL of LB with antibiotics and either 0.5 mM IPTG (pre-IPTG) or 50 ng/mL aTc (pre-aTc) for the overnight growth at 37 °C in a shaker (250 rpm). Next, we prepared 96-well round-bottom plates with minimal M9CA broth, antibiotics, and applicable inducers (IPTG and aTc) with a 2-fold final concentration at a volume of 100 μL per well. We diluted the overnight cultures 1:50 in minimal M9CA broth with antibiotics, and we added 100 μL of this cell dilution to each well (1:1, final cell dilution of 1:100). We incubated the plates at 37

https://doi.org/10.1021/acssynbio.4c00272
ACS Synth. Biol. 2024, 13, 2844−2860

°C and shaking at 650 rpm. After 3 h (and 9 or 12 h for stationary phase tests), we kept the plates on ice for at least 10 min. Then, we added 25 μL of each well to a tube with 475 μL of 1× PBS (5% dilution) and vortexed the tube. We analyzed each tube with a Sony SH800S Cell Sorter. We used filters for mCFP and EYFP. Due to overlap in their fluorescence spectra, we used single fluorescence controls, and the Sony software calculated compensations for each fluorophore. All CFP and YFP values shown here are compensated. For each sample, we recorded 10,000 events. We exported and analyzed the acquired data with FlowJo. We manually created the fluorescence gates. The common existence of OFF cells among the circuits (i.e., cells that express neither CFP nor YFP) generated the need for an OFF gate. We created blank controls for each circuit by transforming the circuit plasmids with an empty reporter plasmid instead of the regular CFP/YFP one. We used these circuits to determine the OFF gate. Next, we created CFP+ and YFP + gates by drawing a diagonal line from top right to bottom left until it reaches the OFF gate. The CFP+ gate is at the upper left of this line, while YFP+ is at the bottom right. We exported geometric mean values and population compositions based on these gates from FlowJo and plotted with MATLAB. For the confocal tests, we also used the Sony SH800S to sort single cells into small Petri dishes (60 mm) containing LB agar. We attached the dishes to the 96-well-plate stage for sorting and later put them into a 37 °C incubator for growth into single colonies.

4.4. Colony Tests. We prepared LB agar plates with antibiotics (50 μg/mL kanamycin, 34 μg/mL chloramphenicol, and 50 μg/mL spectinomycin) and aTc (12.5, 25, 50, or 100 ng/mL). We inoculated cells from single colonies into 5 mL of LB with antibiotics and 0.0625 mM IPTG for overnight growth at 37 °C in a shaker (250 rpm). Next, we diluted the culture 1:100 in 4 mL of LB with antibiotics and 0.0625 mM IPTG, and we grew the culture at 37 °C shaker (250 rpm) until it reached an OD_{600} between 0.7 and 0.8 (approximately 2 h). We then diluted the culture with LB to reach an OD_{600} range between 0.35 and 0.4. Then, we used 1 mL of the diluted outgrowth for serial dilutions until we achieved 1:10,000 and 1:100,000 (outgrowth/LB) ratios. We put plates to warm up in a 37 °C incubator for at least an hour before plating. Then, we plated both 1:10,000 and 1:100,000 dilutions into two equal sets of plates, with 12 glass beads per plate. We wrapped plates in foil to avoid light exposure of aTc, and we placed them in a 37 °C incubator. We took the plates at 24, 28, 32, 44, 52, 76, and 100 h postplating to be imaged in a low-magnification microscope (see 2D Imaging).

4.5. High-Performance Liquid Chromatography Test. To quantify aTc concentration from LB agar fragments, we modified the method from Halling-Sørensen et al.[44] We used an Agilent 1220 Infinity LC instrument and a C-18 chromatographic column (Aeris 3.6 μm Peptide XB-C18 100A LC column 250 mm × 4.6 mm). To start, we directly tested aTc in the following amounts: 5, 2.5, 1.25, 0.625, 0.3125, and 0,15625 μg. From the area under peak, we generated a calibration curve and an equation for aTc quantification for the following tests (Figure S3A). We prepared triplicates of 13 mL of LB agar with aTc at a final concentration of 100 μg/mL. Then, we poured 6 mL of each triplicate into two 24-well plates (1 mL/well). We prepared a total of 36 wells (triplicates for six reads in two plates). To measure the aTc, we transferred the solidified media from each well to separate tubes and diluted each with 9 mL of water. The tubes were kept in the dark and at RT for 2 h. Then, we centrifuged the tubes and filter sterilized the liquid. First, we measured triplicate samples (100 μL injection each) in HPLC before any actual incubation (day 0). Then, we incubated one plate for 48 h at 37 °C (the one without a set of triplicates from day 0 read), while we incubated the other plate at 4 °C to recreate the two possible pretreatments, as described in Colony Tests section. After the first 48 h, we also incubated the 4 °C plate at 37 °C, except for a set of triplicates that was kept at 4 °C until the end of the experiment. We continued the incubation for a total of 6 days to recapitulate the actual experimental setup (see the Colony Tests). Each day starting at day 2, we removed a set of triplicates from each plate, then treated, and injected in the HPLC as explained above. Finally, we quantified aTc by measuring the area under the peak for each run.

4.6. 2D Imaging. We imaged plates with colonies with a stereo microscope (Nikon SMZ800), YFP and CFP fluorescence filters (Chroma #39003 and #39001, respectively), and NIS-Elements software (Nikon). QS and NQS toggles are very different circuits and, therefore, have different fluorescence intensities. For this reason, we used distinct settings for each circuit. We imaged QS toggle colonies with an exposure time of 300 ms for YFP and CFP. While NQS toggle had lower intensities, we used an exposure time of 1 s for both YFP and CFP. We manually imaged each frame for CFP, YFP, and bright field to form a multichannel image. Therefore, not all colonies were captured on all plates. Whenever there were many colonies, we generally picked four frames per plate to cover as many well-separated colonies as possible. We did not image or analyze colonies that were in contact with other colonies. We exported each multichannel image into three separate tiff files. We assembled colony images with Fiji (ImageJ). We used identical minimum and maximum fluorescence values among images in the same figure to enable direct comparison but different values across circuits. For confocal tests, we also imaged colonies with the stereo microscope before any agarose was added. In such images, we used the same exposure time settings for YFP and CFP for QS and NQS toggles (1 s for YFP and 300 ms for CFP). In Fiji, we did not use the same adjusted minimum and maximum fluorescence values for QS and NQS toggles, making these images not directly comparable with respect to their fluorescence intensities.

4.7. Confocal Imaging. We sorted single cells into LB agar plates (see Flow Cytometry), containing antibiotics and aTc (25 or 50 ng/mL). We incubated the plates at 37 °C, wrapped in foil, for different times, ranging from 32 to 72 h. After growth, we covered each colony with approximately 1 mL of an autoclaved 1% agarose solution. For the full colony images, we cut out pieces of agar with agarose-covered colonies, placed them upside down (with agarose on the bottom) on glass coverslips, and took them to the Nikon A1 Confocal microscope. For the perpendicular cross section, we manually cut the pieces in the middle with a blade. We placed the middle part in a glass coverslip for imaging on a Nikon A1 Confocal microscope. In the confocal, we used 405 and 488 nm lasers for excitation of CFP and YFP, respectively. We acquired images with 10× (for full colony Z-stacks) or 20× objective (for slices), resonant scanner, 1 A.U., with denoise capture mode. For Z-stacks, steps varied from 5.1 to 15 μm distance, for a total of 200−500 μm coverage within the *Z* axis. We exported the data into separate tiff files. We made videos with Fiji (ImageJ). We used identical minimum and maximum fluorescence values among images from the same circuit replicates to enable direct comparison, except for figures of slices. We also captured colonies with stereomicroscopy (2D imaging) prior to agarose solution addition for comparison.

https://doi.org/10.1021/acssynbio.4c00272
ACS Synth. Biol. 2024, 13, 2844−2860

4.8. Data Analysis. We performed all data analyses in MATLAB. First, we manually selected all colonies in each frame, and we took the average YFP and CFP fluorescence of four radii (one per direction: N, S, E, and W) per colony. We used the bright field for mask creation and the detection of colonies. We selected regions without colonies for the background, which we subtracted from initial intensities. We saved all of the data from all colonies in the same plate in a matrix per time point. We determined the yellow width by measuring the distance from the center of the colony to the threshold point, in which yellow fluorescence first reaches below 30% of its maximum. We then normalized this distance by dividing by the total colony length (radius), giving results between 0 and 1. To obtain this measure, we made several assumptions: if the maximum YFP value was below a certain arbitrary threshold of 200, the yellow color was considered absent, and the normalized yellow width was 1 divided by total length (close to zero). If the maximum CFP value was below an arbitrary threshold of 300, then the blue color was considered absent, and the normalized yellow width was 1. When the maximum YFP intensity at a particular pixel also had CFP above a very high second threshold of 2000, this probably represented a random patch of yellow cells between blue cells, and we assumed that yellow was absent for purposes of width calculation. Lastly, when blue was absent, and YFP showed small variation between maximum and minimum (below 170), the colony was considered to be completely yellow, and we selected the full colony as the width instead of the highest value. We picked all of these arbitrary threshold values for CFP and YFP through observation. We used them equally for all colonies of both circuits. Furthermore, we normalized each colony's original fluorescence data by its maximum to allow for color overlap analysis. We plotted each pixel from the center to the edge of the colony by its normalized YFP and CFP fluorescence, and they were classified as overlapping only when both YFP and CFP values were above the threshold of 0.3. Some colonies were found to have only one color throughout the entire radius, for example, some of the all-yellow colonies at high aTc concentration. Therefore, such colonies do not show any overlap and can skew the data. To remove single color data (Figure S4), we selected only colonies that had both colors present for at least 25% of pixels. Finally, we compared all data from QS colonies to NQS. Both yellow width and overlap data showed a non-normal distribution; thus, we performed nonparametric statistical tests. We analyzed comparisons among four different aTc concentrations of the same circuit with the Kruskal–Wallis test (nonparametric equivalent to one-way ANOVA), followed by the multiple comparison test (Tukey–Kramer). Meanwhile, we analyzed direct comparison among two sets of data with the Mann–Whitney test (nonparametric equivalent to Student's *t*-test).

4.9. Mathematical Model. *4.9.1. Section I—Bistability in Well-Mixed Environment/Liquid Culture.* In the following, we describe the set of equations modeling the concentrations of LacI and TetR within the cells in the population. We assume that these concentrations are approximately proportional to the fluorescent signals, which are measured experimentally, and use this assumption to compare experimental and modeling results.

4.9.1.1. Single-Cell Model Derivation. We let x(t) and y(t) represent the concentrations of LacI and TetR, respectively. Assuming that the intracellular concentrations of LacI and TetR are proportional to the concentrations of the fluorescent proteins YFP and CFP, respectively. The quantities $x(t)$ and $y(t)$ are then directly related to the experimentally measured fluorescence. We therefore compare the evolutions $x(t)$ and $y(t)$ predicted by our model to the experimentally measured fluorescence signals.

The production of LacI is regulated by a promoter, which can be activated by QS signaling molecules (C14-HSL bound to CinR), and repressed by TetR. Similarly, the production of TetR is activated by the QS signal (C4-HSL bound to RhlR) and repressed by LacI. We denote by $g(t)$ and $h(t)$ the concentrations of QS signals C14-HSL and C4-HSL at time t, respectively. We also assume that LacI and TetR can be produced at maximum rates a_1 and a_2 and are degraded with rate constants γ_1 and γ_2 in addition to the constant dilution at rate γ_d due to cell growth. We can then model the dynamics of the QS toggle using the following system of ODEs describing the intracellular concentrations of LacI and TetR[25,45,46]

$$\dot{x} = a_1\eta_1(y)\phi_1(g) - (\gamma_1 + \gamma_d)x$$

$$\dot{y} = a_2\eta_2(x)\phi_2(h) - (\gamma_2 + \gamma_d)y$$

The repression of the promoter is represented by Hill functions η_1 and η_2, while activation is represented by Hill functions ϕ_1 and ϕ_2. In particular, we set

$$\eta_1(y(t)) = \frac{\theta_y^{n_1}}{\theta_y^{n_1} + y(t)^{n_1}}, \qquad \eta_2(x(t)) = \frac{\theta_x^{n_2}}{\theta_x^{n_2} + x(t)^{n_2}} \tag{4a}$$

and

$$\phi_1(g(t)) = \frac{g(t)}{\theta_g + g(t)}, \qquad \phi_2(h(t)) = \frac{h(t)}{\theta_h + h(t)} \tag{4b}$$

Here, the choice of Hill coefficients is based on the number of monomers in the activator (1 for C14 and C4) and repressor (n_1 = 2 for TetR and n_2 = 4 for LacI).

We model the dynamics of the intercellular QS signals, C14-HSL and C4-HSL, whose activation is repressed by TetR and LacI, by the following equations

$$\dot{g} = a_3\beta_1 + a_3(1 - \beta_1)\eta_1(y) - (\gamma_3 + \gamma_d)g \tag{5a}$$

$$\dot{h} = a_4\beta_2 + a_4(1 - \beta_2)\eta_2(x) - (\gamma_4 + \gamma_d)h \tag{5b}$$

Here, C14-HSL and C4-HSL are produced with maximum rate a_3 and a_4, and degraded at rate γ_3 and γ_4, respectively. Furthermore, let $a_3\beta_1$ and $a_4\beta_2$ represent the base production rate of the QS signals. Settings $\phi_1[g(t)] = 1$ and $\phi_2[h(t)] = 1$ result in equations that describe the NQS toggle.

When exogenous inducers IPTG and aTc, which we denote by U and V, are added to the well-mixed liquid culture, the state of the system can be changed. Following experiments, we will assume that IPTG and aTc are provided at some background concentration level, u_0 and v_0, respectively. The derepression of *lacI*/*tetR* genes is achieved through inducer binding to the opposite corresponding repressors. Let X and Y represent the unbound/free repressors, LacI and TetR, respectively. Let $\hat{X}$ and $\hat{Y}$ denote the inducer-bound complex. The binding activity can be described by the following reaction scheme

$$X + V \xrightarrow{k_{1+}} \hat{X} \tag{6a}$$

$$\hat{X} \xrightarrow{k_{1-}} X + V \tag{6b}$$

$$Y + U \xrightarrow{k_{2+}} \hat{Y} \tag{6c}$$

https://doi.org/10.1021/acssynbio.4c00272
ACS Synth. Biol. 2024, 13, 2844−2860

$$\hat{Y} \xrightarrow{k_{2-}} Y + U \tag{6d}$$

Let $x_b(t)$ and $y_b(t)$ represent the concentrations of bound LacI ($\hat{X}$) and bound TetR ($\hat{Y}$); we then have that

$$\dot{x}_b = k_{1+}x_f v_0 - k_{1-}x_b - (\gamma_1 + \gamma_d)x_b \tag{7a}$$

$$\dot{y}_b = k_{2+}y_f u_0 - k_{2-}y_b - (\gamma_2 + \gamma_d)y_b \tag{7b}$$

Here, $x_f(t)$ and $y_f(t)$ represent the free LacI and TetR. By the conservation law, we have that $x(t) = x_b(t) + x_f(t)$ and $y(t) = y_b(t) + y_f(t)$.

Hence, the set of equations describing the dynamics of the intracellular concentrations of LacI, TetR, the signaling molecules, as well as the concentrations of bound LacI and TetR is given by

$$\dot{x} = a_1\eta_1(y_f)\phi_1(g) - (\gamma_1 + \gamma_d)x \tag{8a}$$

$$\dot{y} = a_2\eta_2(x_f)\phi_2(h) - (\gamma_1 + \gamma_d)y \tag{8b}$$

$$\dot{g} = a_3\beta_1 + a_3(1 - \beta_1)\eta_1(y_f) - (\gamma_3 + \gamma_d)g \tag{8c}$$

$$\dot{h} = a_4\beta_2 + a_4(1 - \beta_2)\eta_2(x_f) - (\gamma_4 + \gamma_d)h \tag{8d}$$

$$\dot{x}_b = k_{1+}x_f v_0 - k_{1-}x_b - (\gamma_1 + \gamma_d)x_b \tag{8e}$$

$$\dot{y}_b = k_{2+}y_f u_0 - k_{2-}y_b - (\gamma_2 + \gamma_d)y_b \tag{8f}$$

4.9.1.2. Nondimensionalization and Bifurcation Analysis. To simplify analysis, we next assume that $\gamma_1 = \gamma_2 = \gamma$. Defining the rescaled time $\tau = (\gamma + \gamma_d)t$, we can nondimensionalize each variable using its corresponding threshold to obtain the following nondimensionalized QS toggle system

$$\frac{d\tilde{x}}{d\tau} = \frac{\tilde{a}_1}{1 + \tilde{y}_f^{n_1}}\frac{\tilde{g}}{1 + \tilde{g}} - \tilde{x} \tag{9a}$$

$$\frac{d\tilde{y}}{d\tau} = \frac{\tilde{a}_2}{1 + \tilde{x}_f^{n_2}}\frac{\tilde{h}}{1 + \tilde{h}} - \tilde{y} \tag{9b}$$

$$\frac{d\tilde{g}}{d\tau} = \frac{\tilde{a}_3}{1 + \tilde{y}_f^{n_1}} - \tilde{\gamma}_3\tilde{g} \tag{9c}$$

$$\frac{d\tilde{h}}{d\tau} = \frac{\tilde{a}_4}{1 + \tilde{x}_f^{n_2}} - \tilde{\gamma}_4\tilde{h} \tag{9d}$$

$$\frac{d\tilde{x}_b}{d\tau} = \tilde{x}_f\tilde{v}_0 - \tilde{k}_{1-}\tilde{x}_b - \tilde{x}_b \tag{9e}$$

$$\frac{d\tilde{y}_b}{d\tau} = \tilde{y}_f\tilde{u}_0 - \tilde{k}_{2-}\tilde{y}_b - \tilde{y}_b \tag{9f}$$

with $\tilde{x}_f = \tilde{x} - \tilde{x}_b$ and $\tilde{y}_f = \tilde{y} - \tilde{y}_b$. Here, the nondimensionalized variables and parameters are

$$\tilde{x} = \frac{x}{\theta_x}; \quad \tilde{y} = \frac{y}{\theta_y}; \quad \tilde{g} = \frac{g}{\theta_g}; \quad \tilde{h} = \frac{h}{\theta_h}; \quad \tilde{x}_b = \frac{x_b}{\theta_x}; \quad \tilde{y}_b = \frac{y_b}{\theta_y}; \quad \tilde{x}_f = \frac{x_f}{\theta_x}; \quad \tilde{y}_f = \frac{y_f}{\theta_y}$$

$$\tilde{a}_1 = \frac{a_1}{\theta_x(\gamma + \gamma_d)}; \quad \tilde{a}_2 = \frac{a_2}{\theta_y(\gamma + \gamma_d)}; \quad \tilde{a}_3 = \frac{a_3}{\theta_g(\gamma + \gamma_d)}; \quad \tilde{a}_4 = \frac{a_4}{\theta_h(\gamma + \gamma_d)}$$

$$\tilde{\gamma}_3 = \frac{\gamma_3 + \gamma_d}{\gamma + \gamma_d}; \quad \tilde{\gamma}_4 = \frac{\gamma_4 + \gamma_d}{\gamma + \gamma_d}; \quad \tilde{v}_0 = \frac{k_{1+}v_0}{\gamma + \gamma_d}; \quad \tilde{u}_0 = \frac{k_{2+}u_0}{\gamma + \gamma_d}; \quad \tilde{k}_{1-} = \frac{k_{1-}}{\gamma + \gamma_d}; \quad \tilde{k}_{2-} = \frac{k_{2-}}{\gamma + \gamma_d}$$

Equation 9a describes the NQS toggle system after removing (9c and 9d) and setting $\tilde{g}/(1 + \tilde{g}) = 1$ and $\tilde{h}/(1 + \tilde{h}) = 1$ in (9a and 9b). The nondimensionalization shows that, in the NQS toggle system, the effective synthesis rate of the repressor, $\tilde{a}_1$ and $\tilde{a}_2$, is determined by a balance between production, degradation, dilution, and the repression threshold. In the QS system, the effective synthesis rate of the repressors is modified by the QS signal profile. That is

$$s_1(t) = \frac{\tilde{a}_1\tilde{g}(t)}{1 + \tilde{g}(t)}; \quad s_2(t) = \frac{\tilde{a}_2\tilde{h}(t)}{1 + \tilde{h}(t)}$$

To understand how the different parameters impact the equilibria of the system, we first obtained the equilibria by setting the derivatives in eqs 9a−0. Denoting the equilibrium values of the different dynamical variables by a star, we have that $\tilde{x}_f^*$ and $\tilde{y}_f^*$ satisfy

$$F_1(\tilde{x}_f^*, \tilde{y}_f^*) := \frac{s_1}{1 + \tilde{y}_f^{*n_1}} - \tilde{x}_f^* = 0 \tag{10a}$$

$$F_2(\tilde{x}_f^*, \tilde{y}_f^*) := \frac{s_2}{1 + \tilde{x}_f^{*n_2}} - \tilde{y}_f^* = 0 \tag{10b}$$

with

$$\hat{s}_1 = \frac{\tilde{a}_1}{1 + \tilde{v}_0}\frac{\tilde{g}^*}{1 + \tilde{g}^*}, \quad \hat{s}_2 = \frac{\tilde{a}_2}{1 + \hat{u}_0}\frac{\tilde{h}^*}{1 + \tilde{h}^*}$$

and

$$\tilde{v}_0 = \frac{\tilde{v}_0}{\tilde{k}_{1-} + 1}, \quad \tilde{u}_0 = \frac{\tilde{u}_0}{\tilde{k}_{2-} + 1}$$

Let $\mathcal{L} \subset \mathbb{R}^2$ represent the bifurcation curve in the $(\hat{s}_1, \hat{s}_2)$ parameter space, that is, the curve in the parameter space at which the behavior of the system changes qualitatively. Here, crossing the bifurcation curve leads to a change in the number of equilibria and/or their stability.[47] Except for the steady-state condition described in eqs 8a and 8b, points on the bifurcation curve $\mathcal{L}$ additionally must satisfy a matching slope condition.[47] That is

$$-\frac{\partial F_1/\partial \tilde{x}_f^*}{\partial F_1/\partial \tilde{y}_f^*}\bigg|_{(\hat{x}_f^*, \hat{y}_f^*)} = -\frac{\partial F_2/\partial \tilde{x}_f^*}{\partial F_2/\partial \tilde{y}_f^*}\bigg|_{(\hat{x}_f^*, \hat{y}_f^*)}$$

After some algebra, the above condition can be simplified as follows

https://doi.org/10.1021/acssynbio.4c00272
ACS Synth. Biol. 2024, 13, 2844−2860

$$\hat{s}_1\hat{s}_2 = n_1 n_2 \hat{x}_f^{*n_2+1}\hat{y}_f^{*n_1+1} \tag{10c}$$

Solving system (10) numerically gives us the cusp bifurcation curve $\mathcal{L}$ in the $(\hat{s}_1, \hat{s}_2)$ space, as shown in Figure 2E. All the parameter values used in the plots are listed in Table S2.

4.9.2. Section II—Spatial−Temporal Dynamics of the NQS and QS Colony. Using the model of the intracellular dynamics developed above, we next describe a model of the spatiotemporal dynamics of the corresponding LacI and TetR quantities in a growing bacterial colony.

4.9.2.1. Domain. The domain, $\Omega \subseteq \mathbb{R}^3$, on which we define the partial differential equation (PDE) model consists of two different subdomains, $\Omega = \Omega_1 \cup \Omega_2$, with Ω_1 representing the part of the domain occupied by the bacterial colony and Ω_2 representing the part occupied by the agar. The agar plate takes the shape of a cylinder, and we assume that the colony takes the shape of a cone,[40] as show in Figure S7A. Assuming radial symmetry, we can reduce the 3D domain to a 2D slice.

There are two different types of boundaries: the inner boundary, represented by $\partial\Omega^{in}$, and the outer boundary, represented by $\partial\Omega$. The inner boundary is the interface between the colony subdomain, Ω_1, and the agar subdomain, Ω_2. The outer boundary is the union of the colony−air interface and the agar−plate interface.

The colony is observed experimentally over tens of hours, during which it can grow substantially. We therefore included colony growth in the model. Previously, Warren et al. have identified three phases of colony expansion:[40] the initial monolayer phase (0−13 h); the establishment phase (14−24 h); and the flattening phase (24 h). In the establishment phase, growth in both height and radius is linear, as cells predominantly divide in the active growing region consisting of a thin disk at the bottom of the colony of approximate height H_{AGL} = 10 μm. During the flattening phase, radial growth is still linear, while the increase in height slows down.

In our case, the observed pattern in both the NQS and QS colonies is driven by diffusive signals. Since the size of the colony is much smaller than the characteristic length scale of signal diffusion, a detailed quantitative description on how the colony grows vertically does not matter much. Therefore, for simplicity, we assume that the colony expands linearly in both radius and height with a thin actively growing layer on the bottom. These assumptions together imply a fixed aspect ratio in colony height vs radius. In our simulation, the continuous growth of the colony is discretized by adding slabs of uniform heights and linearly increasing the radius every unit of time. In particular, experimentally, the radius of the colony by the end of 100 h is approximately 4 mm, giving a linear radius growth rate of v_r = 40 μm/h. Moreover, the cross-sectional images of the colony show that at different times of colony expansion, the height to radius ratio ranges from 1:7 to 1:12. For simplicity, we assume a fixed ratio of the height to base in the triangular slice to be 1:10, which leads to a linear height growth rate of v_h = 4 μm/h.

As shown in Figure S7B, based on growth assumption at different locations, we divide the colony subdomain Ω_1 into three different regions: top (Ω_{11}), base (Ω_{12}), and rim (Ω_{13}). In particular, the triangular top, defined as $\Omega_{11} = \{(r,z) \in \Omega_1 | z \geq H_{AGL}\}$, does not grow. Let R_k represent the radial length of the colony at the end of time intervals (t_{k-1},t_k). The rectangular base, defined as $\Omega_{12} = \{(r,z) \in \Omega_1 | r \leq R_k, z \leq H_{AGL}\}$, grows linearly only in the vertical direction. The triangular rim, defined as $\Omega_{13} = \{(r,z) \in \Omega_1 | r \geq R_k\}$, grows linearly in both the vertical and radial directions.

Let T be the time that it takes for the colony to grow H_{AGL} in the vertical direction. Here, the ratio is $T = H_{AGL}/v_h$ = 150 min. Let S_k^{12} represent the area of the top region, Ω_{12}, at the end of time interval (t_{k-1},t_k), where $S_k^{12} = H_{AGL}R_k$. Then, we have that

$$\frac{S_{k+1}^{12} - S_k^{12}}{\Delta t} = \frac{\Delta H}{\Delta t}R_k = \frac{H_{AGL}}{T}R_k = \frac{1}{T}S_k^{12}$$

Similarly, let S_k^{13} represent the area of the rim region, Ω_{13}, at the end of time interval (t_{k-1},t_k), where $S_k^{13} = \kappa H_{AGL}^2/2$, with κ representing the fixed radius-height ratio of the colony. Then, we have

$$\begin{aligned}\frac{S_{k+1}^{13} - S_k^{13}}{\Delta t} &= \frac{\Delta H}{\Delta t}\kappa\left(H_{AGL} + \frac{1}{2}\Delta H\right)\\ &= \frac{H_{AGL}}{T}\kappa\left(H_{AGL} + \frac{1}{2}\Delta H\right)\\ &= \frac{2}{T}S_k^{13} + O(\Delta H)\end{aligned}$$

Therefore, we can approximate the expansion factor of the rim region, Ω_{13}, by $2/T$, which is twice as fast as the expansion rate for the base region, Ω_{12}. Let $\gamma_d = 1/T$, we then get the following chemical dilution rate from colony expansion in the different regions

$$\gamma_d(X) = \begin{cases} 0, & X \in \Omega_{11} \\ \gamma_d, & X \in \Omega_{12} \\ 2\gamma_d, & X \in \Omega_{13} \end{cases}$$

4.9.2.2. PDE Model. Let $u(X,t)$ represent the aTc concentration at time t and location $X \in \Omega$. The inducer, aTc, is initially supplied in the agar, which then diffuses into the colony and reacts with TetR in different cells. The reaction occurring within the cells in the colony can be modeled using eqs 6c and 6d. We assume that when the aTc−TetR complex, $\hat{Y}$, is being degraded by the enzyme ClpXP, a portion $\alpha \in [0,1]$ of the aTc returns to the cell from the complex.[48] That is

$$\hat{Y} \xrightarrow{\alpha(\gamma_2+\gamma_d(X))} \phi + U$$

putting everything together, for the concentrations of

x: [LacI]; y_f: [freeTetR];

y_b: [boundTetR]; g: [C14]; h: [C4];

u: [aTc]

with $y = y_f + y_b$, and the superscript represent different subdomain, we obtain a diffusion−reaction model we describe next.

In the colony domain, $X \in \Omega_1$, the various concentrations evolve according to

$$\frac{\partial x}{\partial t} = a_1\eta_1(y_f)\phi_1(g) - (\gamma_1 + \gamma(X))x \tag{11a}$$

$$\frac{\partial y}{\partial t} = a_2\eta_2(x_f)\phi_2(h) - (\gamma_2 + \gamma(X))y \tag{11b}$$

$$\frac{\partial y_b}{\partial t} = k_{2+}u^c y_f - k_{2-}y_b - (\gamma_2 + \gamma(X))y_b \tag{11c}$$

https://doi.org/10.1021/acssynbio.4c00272
ACS Synth. Biol. 2024, 13, 2844−2860

$$\frac{\partial g^{c}}{\partial t} = D_1^{c}\Delta g^{c} + a_3\beta_1 + a_3(1-\beta_3)\eta_1(y_f) - (\gamma_3 + \gamma(X))g^{c} \tag{11d}$$

$$\frac{\partial h^{c}}{\partial t} = D_2^{c}\Delta h^{c} + a_4\beta_4 + a_4(1-\beta_4)\eta_2(x_f) - (\gamma_4 + \gamma(X))h^{c} \tag{11e}$$

$$\frac{\partial u^{c}}{\partial t} = D_3^{c}\Delta u^{c} - k_{2+}u^{c}y_f + k_{2-}y_b + \alpha(\gamma_2 + \gamma_d(X))y_b - (\gamma_5 + \gamma(X))u^{c} \tag{11f}$$

In the agar domain, Ω_2, we have

$$\frac{\partial g^{a}}{\partial t} = D_1^{a}\Delta g^{a} - \gamma_3 g^{a} \tag{11g}$$

$$\frac{\partial h^{a}}{\partial t} = D_2^{a}\Delta h^{a} - \gamma_4 h^{a} \tag{11h}$$

$$\frac{\partial u^{a}}{\partial t} = D_3^{a}\Delta u^{a} - \gamma_5 u^{a} \tag{11i}$$

Here, D_i^{a} denotes the signal diffusion coefficient in agar, for different chemicals C14, C4, and aTc indexed by $i = 1, 2$, and 3, respectively. Due to the crowdedness of the colony, we assume that signal diffusion coefficients in the colony, D_i^{c}, satisfies $D_i^{c} < D_i^{a}$. In particular, it has been shown that GFP diffuses 10 times faster in water ($D_{GFP}^{aqua} \approx 87\ \mu m^2/s$),[49] compared with in the cytoplasm ($D_{GFP}^{cyto} \approx 8\ \mu m^2/s$).[50] Therefore, we set $D_i^{a} = 10D_i^{c}$. Since aTc has a lower molecular weight than GFP, we assume that the aTc diffusion coefficient in agar is $D_1^{a} = 400\ \mu m^2/s$. It has been reported that the effective diffusion coefficients of C14 and C4 are $D_{C14} \approx 83\ \mu m^2/s$ and $D_{C4} \approx 1810\ \mu m^2/s$.[19] Here, we set the diffusion coefficients in agar to $D_2^{a} = 10^2\ \mu m^2/s$ and $D_3^{a} = 10^3\ \mu m^2/s$ for C14 and C4, respectively.

For the diffusible chemicals, $C = g$, h, or u, we also use the following inner and outer boundary conditions.

$$C^{a}(X, t)|_{X\in\partial\Omega^{in}} = C^{c}(X, t)|_{X\in\partial\Omega^{in}} \tag{11j}$$

$$\boldsymbol{n}\cdot D_i^{a}\nabla C^{a}(X, t)|_{X\in\partial\Omega^{in}} = -\boldsymbol{n}\cdot D_i^{c}\nabla C^{c}(X, t)|_{X\in\partial\Omega^{in}} \tag{11k}$$

$$\boldsymbol{n}\cdot D_i^{a/c}\nabla C^{a/c}(X, t)|_{X\in\partial\Omega} = 0 \tag{11l}$$

We used the radial symmetry of the 3D domain to reduce it to an equivalent 2D model. Let r and z represent the independent variables denoting the radius and height coordinates inside the colony. We then observe that the Laplacian operator acts on $C = g$, h, or u as

$$\Delta C = \frac{1}{r}\frac{\partial}{\partial r}\left(r\frac{\partial C}{\partial r}\right) + \frac{\partial C}{\partial z}$$

5. PARAMETERS AND SIMULATION

We assume that the tagged degradation gives a half-life of 7 min for intercellular species.[33] This leads to degradation rates of LacI and TetR of $\gamma = \gamma_1 = \gamma_2 = \ln(2)/7\ min^{-1}$. It has been reported that the degradation rate of AHL ranges from zero (no detectable degradation at 32 h) to a half-life of 8 h depending on environmental factors such as temperature and pH value.[39] For our experimental condition, we assume that the half-life of C14 and C4 is 24 h, corresponding to degradation rates of $\gamma_3 = \gamma_4 = \ln(2)/24\ h^{-1}$. The production rates of each species, a_i, with $i = 1,..,4$ along with their corresponding threshold of activation (EC50)/repression (IC50) parameters θ_j, with $j = \{x,y,g,h\}$, were chosen so that the nondimensionalized parameters, $\tilde{a}_i$, give a match with experimentally observed patterns. We also set the basal production level of the AHL signals to $\beta_1 = 0.2$ and $\beta_1 = 0.5$, for C14 and C4, respectively. It has been reported that aTc binds with TetR at a rate of $k_+ = 0.06/nM/min$.[48] As shown in Figure 1E,G, aTc can induce the yellow state at a concentration of 1 ng/mL in the NQS toggle and at approximately 10 ng/mL in the QS toggle case. Therefore, we set $k_+ = k{\cdot}0.06\ nM^{-1}\ min^{-1}$, with $k = 1$ in the NQS toggle and $k = 10$ in the QS toggle. We set the unbinding rate to $k_- = k_+/k_A$, with association constant $k_A = 10/nM$.[51] When the aTc−TetR complex is degraded by ClpXP, we assume that $\alpha = 0.8$, the portion of the aTc in the complex returns back to the cell. All parameters used in Figure 7C,D are the same as those used in Figure 7B except the following: in Figure 7C, a pulse of $\gamma = \ln(2)/5.178\ min^{-1}$ between $t = 23.25$ h and $t = 25.575$ h is applied; in Figure 7D, synthesis rates are reduced to $a_1 = 80$ nM/min and $a_2 = 120$ nM/min.

We simulate the PDE−ODE model, described by eq 11a, using MATLAB. To reduce interpolation error, we took the following approach: first, over $\delta t = 1$ min time intervals, the PDEs were solved using the PDE Toolbox and the ODEs were solved using ode15s at each mesh point using the solution from the previous time step as initial conditions. Second, the mesh for subdomain Ω_{11}, the top of the colony, was kept the same between each update of the colony size at every $\Delta t = 15$ min. Meanwhile, at each colony growth update time point $t = t_k$, as shown in Figure S1B, mesh points in the bottom layer (Ω_{12} and Ω_{13}) were initialized by interpolating the solution at $t = t_k^-$ with the coordinates of the mesh points linearly stretched, as shown in Figure S1C. All of the parameter values used are listed in Table S2.

■ ASSOCIATED CONTENT

Supporting Information

The Supporting Information is available free of charge at https://pubs.acs.org/doi/10.1021/acssynbio.4c00272.

Induction curves of circuit variations of the QS toggle; flow cytometry data for different time durations; temperature effect in aTc degradation; extra representation of pixel overlap analysis; distinct behaviors of QS toggle in solid media; schematics of the 3D domain and colony expansion used in numerical simulations; list of genetic circuits and plasmids; list of parameters used in simulations; and movie legends (PDF)

QS toggle simulation (MP4)

NQS toggle simulation (MP4)

■ AUTHOR INFORMATION

Corresponding Authors

Krešimir Josić − *Department of Mathematics, University of Houston, Houston, Texas 77204, United States*; Email: josic@math.uh.edu

Matthew R. Bennett − *Department of Biosciences, Rice University, Houston, Texas 77005, United States; Department of Bioengineering, Rice University, Houston, Texas 77005, United States*; orcid.org/0000-0002-4975-8854; Email: matthew.bennett@rice.edu

Authors

Bárbara de Freitas Magalhães − *Department of Biosciences, Rice University, Houston, Texas 77005, United States*

https://doi.org/10.1021/acssynbio.4c00272
ACS Synth. Biol. 2024, 13, 2844−2860

Gaoyang Fan − *Department of Mathematics, University of Houston, Houston, Texas 77204, United States;* orcid.org/0000-0001-6149-2131

Eduardo Sontag − *Department of Bioengineering and Department of Electrical and Computer Engineering, Northeastern University, Boston, Massachusetts 02115, United States;* orcid.org/0000-0001-8020-5783

Complete contact information is available at: https://pubs.acs.org/10.1021/acssynbio.4c00272

Author Contributions

⊥B.F.M. and G.F. contributed equally. Author contributions: conceptualization, B.F.M., G.F., E.D.S., K.J., and M.R.B.; methodology, B.F.M., G.F., E.D.S., K.J., and M.R.B; validation, B.F.M. and M.R.B.; data curation, B.F.M.; investigation, B.F.M. and G.F.; formal analysis, B.F.M. and G.F; visualization, B.F.M. and G.F.; writing—original draft, B.F.M., G.F., K.J., and M.R.B.; writing—review and editing, B.F.M., G.F., E.D.S., K.J., and M.R.B.; software, G.F.; project administration, B.F.M., G.F., K.J., and M.R.B.; funding acquisition, B.F.M., K.J., and M.R.B.; and supervision, K.J. and M.R.B.

Notes

The authors declare no competing financial interest.

■ ACKNOWLEDGMENTS

B.F.M. acknowledges support from Brazilian Coordination for the Improvement of Higher Education Personnel (CAPES), through the Science without Borders (SwB) fellowship. G.F. and K.J. acknowledge support from NSF (1936770). K.J. acknowledges support from MCB-1936770. M.R.B. acknowledges support from the Welch Foundation (C-1729), the National Institutes of Health (R01GM144959), and the NSF (MCB-1936774). E.D.S. acknowledges support from grants NSF/DMS-2052455 and AFOSR FA9550-21-1-0289. The authors also acknowledge the use of resources of the Shared Equipment Authority at Rice University for this work. The computational work was completed in part with resources provided by the Research Computing Data Core at the University of Houston.

■ REFERENCES

(1) Benner, S. A.; Sismour, A. M. Synthetic Biology. *Nat. Rev. Genet.* **2005**, *6* (7), 533−543.
(2) Cameron, D. E.; Bashor, C. J.; Collins, J. J. A Brief History of Synthetic Biology. *Nat. Rev. Microbiol.* **2014**, *12* (5), 381−390.
(3) Cheng, A. A.; Lu, T. K. Synthetic Biology: An Emerging Engineering Discipline. *Annu. Rev. Biomed. Eng.* **2012**, *14* (1), 155−178.
(4) Church, G. M.; Elowitz, M. B.; Smolke, C. D.; Voigt, C. A.; Weiss, R. Realizing the Potential of Synthetic Biology. *Nat. Rev. Mol. Cell Biol.* **2014**, *15* (4), 289−294.
(5) Callura, J. M.; Cantor, C. R.; Collins, J. J. Genetic Switchboard for Synthetic Biology Applications. *Proc. Natl. Acad. Sci. U.S.A.* **2012**, *109* (15), 5850−5855.
(6) Khalil, A. S.; Collins, J. J. Synthetic Biology: Applications Come of Age. *Nat. Rev. Genet.* **2010**, *11* (5), 367−379.
(7) McCarty, N. S.; Ledesma-Amaro, R. Synthetic Biology Tools to Engineer Microbial Communities for Biotechnology. *Trends Biotechnol.* **2019**, *37* (2), 181−197.
(8) Xia, P.-F.; Ling, H.; Foo, J. L.; Chang, M. W. Synthetic Genetic Circuits for Programmable Biological Functionalities. *Biotechnol. Adv.* **2019**, *37* (6), 107393.
(9) Davies, J. A.; Glykofrydis, F. Engineering Pattern Formation and Morphogenesis. *Biochem. Soc. Trans.* **2020**, *48* (3), 1177−1185.
(10) Weisenberger, M. S.; Deans, T. L. Bottom-up Approaches in Synthetic Biology and Biomaterials for Tissue Engineering Applications. *J. Ind. Microbiol. Biotechnol.* **2018**, *45* (7), 599−614.
(11) Cachat, E.; Liu, W.; Davies, J. A. Synthetic Self-patterning and Morphogenesis in Mammalian Cells: A Proof-of-concept Step towards Synthetic Tissue Development. *Eng. Biol.* **2017**, *1* (2), 71−76.
(12) Grant, P. K.; Szep, G.; Patange, O.; Halatek, J.; Coppard, V.; Csikász-Nagy, A.; Haseloff, J.; Locke, J. C. W.; Dalchau, N.; Phillips, A. Interpretation of Morphogen Gradients by a Synthetic Bistable Circuit. *Nat. Commun.* **2020**, *11* (1), 5545.
(13) Kim, H.; Jin, X.; Glass, D. S.; Riedel-Kruse, I. H. Engineering and Modeling of Multicellular Morphologies and Patterns. *Curr. Opin. Genet. Dev.* **2020**, *63*, 95−102.
(14) Santos-Moreno, J.; Schaerli, Y. Using Synthetic Biology to Engineer Spatial Patterns. *Adv. Biosyst.* **2019**, *3* (4), 1800280.
(15) Sekine, R.; Shibata, T.; Ebisuya, M. Synthetic Mammalian Pattern Formation Driven by Differential Diffusivity of Nodal and Lefty. *Nat. Commun.* **2018**, *9* (1), 5456.
(16) Turing, A. M. The Chemical Basis of Morphogenesis. *Philos. Trans. R. Soc. Lond. B Biol. Sci.* **1952**, *237* (641), 37−72.
(17) Wolpert, L. Positional Information and the Spatial Pattern of Cellular Differentiation. *J. Theor. Biol.* **1969**, *25* (1), 1−47.
(18) Diambra, L.; Senthivel, V. R.; Menendez, D. B.; Isalan, M. Cooperativity To Increase Turing Pattern Space for Synthetic Biology. *ACS Synth. Biol.* **2015**, *4* (2), 177−186.
(19) Karig, D.; Martini, K. M.; Lu, T.; DeLateur, N. A.; Goldenfeld, N.; Weiss, R. Stochastic Turing Patterns in a Synthetic Bacterial Population. *Proc. Natl. Acad. Sci. U.S.A.* **2018**, *115* (26), 6572−6577.
(20) Cao, Y.; Ryser, M. D.; Payne, S.; Li, B.; Rao, C. V.; You, L. Collective Space-Sensing Coordinates Pattern Scaling in Engineered Bacteria. *Cell* **2016**, *165* (3), 620−630.
(21) Curatolo, A. I.; Zhou, N.; Zhao, Y.; Liu, C.; Daerr, A.; Tailleur, J.; Huang, J. Cooperative Pattern Formation in Multi-Component Bacterial Systems through Reciprocal Motility Regulation. *Nat. Phys.* **2020**, *16* (11), 1152−1157.
(22) Liu, C.; Fu, X.; Liu, L.; Ren, X.; Chau, C. K. L.; Li, S.; Xiang, L.; Zeng, H.; Chen, G.; Tang, L.-H.; Lenz, P.; Cui, X.; Huang, W.; Hwa, T.; Huang, J.-D. Sequential Establishment of Stripe Patterns in an Expanding Cell Population. *Science* **2011**, *334* (6053), 238−241.
(23) Payne, S.; Li, B.; Cao, Y.; Schaeffer, D.; Ryser, M. D.; You, L. Temporal Control of Self-organized Pattern Formation without Morphogen Gradients in Bacteria. *Mol. Syst. Biol.* **2013**, *9* (1), 697.
(24) Potvin-Trottier, L.; Lord, N. D.; Vinnicombe, G.; Paulsson, J. Synchronous Long-Term Oscillations in a Synthetic Gene Circuit. *Nature* **2016**, *538* (7626), 514−517.
(25) Gardner, T. S.; Cantor, C. R.; Collins, J. J. Construction of a Genetic Toggle Switch in Escherichia Coli. *Nature* **2000**, *403* (6767), 339−342.
(26) Briscoe, J.; Small, S. Morphogen Rules: Design Principles of Gradient-Mediated Embryo Patterning. *Development* **2015**, *142* (23), 3996−4009.
(27) Nasiadka, A.; Dietrich, B. H.; Krause, H. M. Anterior-Posterior Patterning in the Drosophila Embryo. *Adv. Dev. Biol. Biochem.* **2002**, *12*, 155−204.
(28) Struhl, G. Differing Strategies for Organizing Anterior and Posterior Body Pattern in Drosophila Embryos. *Nature* **1989**, *338* (6218), 741−744.
(29) Alaynick, W. A.; Jessell, T. M.; Pfaff, S. L. SnapShot: Spinal Cord Development. *Cell* **2011**, *146* (1), 178−178.e1.
(30) Dessaud, E.; McMahon, A. P.; Briscoe, J. Pattern Formation in the Vertebrate Neural Tube: A Sonic Hedgehog Morphogen-Regulated Transcriptional Network. *Development* **2008**, *135* (15), 2489−2503.
(31) Gomez, M. M.; Arcak, M. A Tug-of-War Mechanism for Pattern Formation in a Genetic Network. *ACS Synth. Biol.* **2017**, *6* (11), 2056−2066.
(32) Nikolaev, E. V.; Sontag, E. D. Quorum-Sensing Synchronization of Synthetic Toggle Switches: A Design Based on Monotone Dynamical Systems Theory. *PLoS Comput. Biol.* **2016**, *12* (4), No. e1004881.

(33) Chen, Y.; Kim, J. K.; Hirning, A. J.; Josić, K.; Bennett, M. R. Emergent Genetic Oscillations in a Synthetic Microbial Consortium. *Science* **2015**, *349* (6251), 986−989.
(34) Lithgow, J. K.; Wilkinson, A.; Hardman, A.; Rodelas, B.; Wisniewski-Dyé, F.; Williams, P.; Downie, J. A. The Regulatory Locus *CinRI* in *Rhizobium Leguminosarum* Controls a Network of Quorum-sensing Loci. *Mol. Microbiol.* **2000**, *37* (1), 81−97.
(35) Pesci, E. C.; Pearson, J. P.; Seed, P. C.; Iglewski, B. H. Regulation of Las and Rhl Quorum Sensing in Pseudomonas Aeruginosa. *J. Bacteriol.* **1997**, *179* (10), 3127−3132.
(36) Barbier, I.; Perez-Carrasco, R.; Schaerli, Y. Controlling Spatiotemporal Pattern Formation in a Concentration Gradient with a Synthetic Toggle Switch. *Mol. Syst. Biol.* **2020**, *16* (6), No. e9361.
(37) Lugagne, J.-B.; Sosa Carrillo, S.; Kirch, M.; Köhler, A.; Batt, G.; Hersen, P. Balancing a Genetic Toggle Switch by Real-Time Feedback Control and Periodic Forcing. *Nat. Commun.* **2017**, *8* (1), 1671.
(38) Wang, L.; Walker, B. L.; Iannaccone, S.; Bhatt, D.; Kennedy, P. J.; Tse, W. T. Bistable Switches Control Memory and Plasticity in Cellular Differentiation. *Proc. Natl. Acad. Sci. U.S.A.* **2009**, *106* (16), 6638−6643.
(39) Politi, N.; Pasotti, L.; Zucca, S.; Casanova, M.; Micoli, G.; Cusella De Angelis, M. G.; Magni, P. Half-Life Measurements of Chemical Inducers for Recombinant Gene Expression. *J. Biol. Eng.* **2014**, *8* (1), 5.
(40) Warren, M. R.; Sun, H.; Yan, Y.; Cremer, J.; Li, B.; Hwa, T. Spatiotemporal Establishment of Dense Bacterial Colonies Growing on Hard Agar. *Elife* **2019**, *8*, No. e41093.
(41) Riglar, D. T.; Richmond, D. L.; Potvin-Trottier, L.; Verdegaal, A. A.; Naydich, A. D.; Bakshi, S.; Leoncini, E.; Lyon, L. G.; Paulsson, J.; Silver, P. A. Bacterial Variability in the Mammalian Gut Captured by a Single-Cell Synthetic Oscillator. *Nat. Commun.* **2019**, *10* (1), 4665.
(42) Xiong, L.; Cao, Y.; Cooper, R.; Rappel, W.-J.; Hasty, J.; Tsimring, L. Flower-like Patterns in Multi-Species Bacterial Colonies. *Elife* **2020**, *9*, No. e48885.
(43) Chen, Y.; Ho, J. M. L.; Shis, D. L.; Gupta, C.; Long, J.; Wagner, D. S.; Ott, W.; Josić, K.; Bennett, M. R. Tuning the Dynamic Range of Bacterial Promoters Regulated by Ligand-Inducible Transcription Factors. *Nat. Commun.* **2018**, *9* (1), 64.
(44) Halling-Sørensen, B.; Sengeløv, G.; Tjørnelund, J. Toxicity of Tetracyclines and Tetracycline Degradation Products to Environmentally Relevant Bacteria, Including Selected Tetracycline-Resistant Bacteria. *Arch. Environ. Contam. Toxicol.* **2002**, *42* (3), 263−271.
(45) Nordholt, N.; van Heerden, J.; Kort, R.; Bruggeman, F. J. Effects of Growth Rate and Promoter Activity on Single-Cell Protein Expression. *Sci. Rep.* **2017**, *7* (1), 6299.
(46) Zong, D. M.; Cinar, S.; Shis, D. L.; Josić, K.; Ott, W.; Bennett, M. R. Predicting Transcriptional Output of Synthetic Multi-Input Promoters. *ACS Synth. Biol.* **2018**, *7* (8), 1834−1843.
(47) Kuznetsov, Y. A. *Elements of Applied Bifurcation Theory*; Applied Mathematical Sciences: Springer New York: New York, NY, 2004; Vol. *112*..
(48) Nevozhay, D.; Adams, R. M.; Murphy, K. F.; Josić, K.; Balázsi, G. Negative Autoregulation Linearizes the Dose−Response and Suppresses the Heterogeneity of Gene Expression. *Proc. Natl. Acad. Sci. U.S.A.* **2009**, *106* (13), 5123−5128.
(49) Swaminathan, R.; Hoang, C. P.; Verkman, A. S. Photobleaching Recovery and Anisotropy Decay of Green Fluorescent Protein GFP-S65T in Solution and Cells: Cytoplasmic Viscosity Probed by Green Fluorescent Protein Translational and Rotational Diffusion. *Biophys. J.* **1997**, *72* (4), 1900−1907.
(50) Elf, J.; Li, G.-W.; Xie, X. S. Probing Transcription Factor Dynamics at the Single-Molecule Level in a Living Cell. *Science* **2007**, *316* (5828), 1191−1194.
(51) Kintrup, M.; Schubert, P.; Kunz, M.; Chabbert, M.; Alberti, P.; Bombarda, E.; Schneider, S.; Hillen, W. Trp Scanning Analysis of Tet Repressor Reveals Conformational Changes Associated with Operator and Anhydrotetracycline Binding. *Eur. J. Biochem.* **2000**, *267* (3), 821−829.

https://doi.org/10.1021/acssynbio.4c00272
ACS Synth. Biol. 2024, 13, 2844−2860

Supporting Information: Pattern formation and bistability in a synthetic intercellular genetic toggle

Bárbara de Freitas Magalhães[1,5], Gaoyang Fan[2,5], Eduardo Sontag[3], Krešimir Josić[2,*], Matthew R. Bennett[1,4,*]

1. Department of Biosciences, Rice University, Houston, TX, 77005, USA

2. Department of Mathematics, University of Houston, Houston, TX, 77204, USA

3. Department of Bioengineering, Department of Electrical and Computer Engineering, Northeastern University, Boston, MA, 02115, USA

4. Department of Bioengineering, Rice University, Houston, TX, 77005, USA

5. These authors contributed equally

*Correspondence: josic@math.uh.edu; matthew.bennett@rice.edu

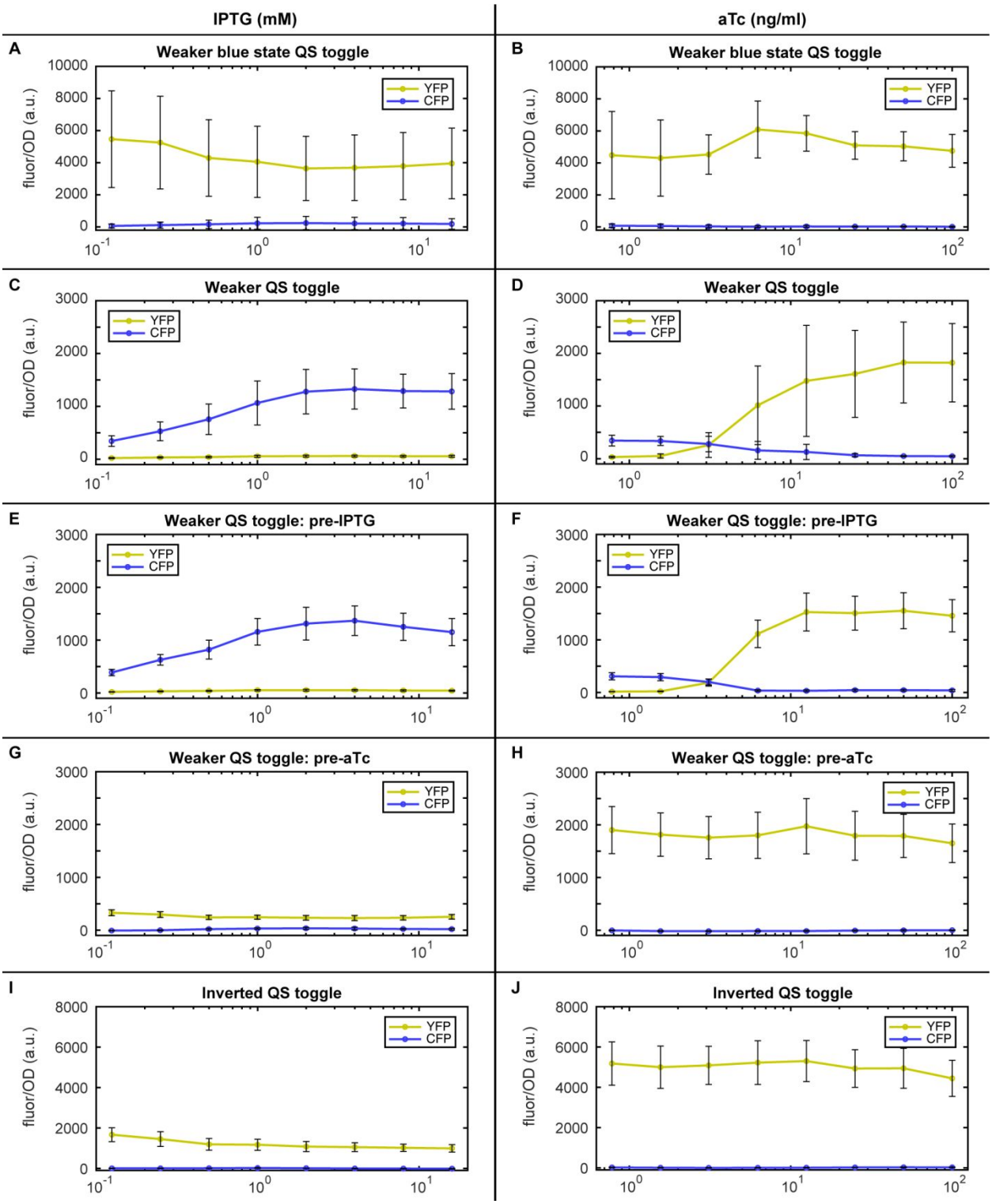

Figure S1: Induction curves of circuit variations of the QS toggle. We obtained the Weaker Blue State by using lower strength promoters for *tetR* and *cfp* genes. We obtained the Weaker QS toggle by using lower strength promoters for the circuit genes, except both QS genes which were kept the same. We obtained the Inverted QS toggle by using the same lower strength promoters but reversing the QS network connected to each state: now, the rhlR/I network activates the yellow state, and cinR/I the blue state (see Table S1). **A, B)** Induction curves of Weaker Blue State QS

toggle with IPTG (A) and aTc (B) in liquid culture. **C, D)** Induction curves of Weaker QS toggle with IPTG (C) and aTc (D) in liquid culture. **E, F)** Induction curves of Weaker QS toggle with IPTG (E) and aTc (F) in liquid culture, in which cells were pre-treated with IPTG. **G, H)** Induction curves of weaker QS toggle with IPTG (G) and aTc (H) in liquid culture, in which cells were pre-treated with aTc. **I, J)** Induction curves of Inverted QS toggle with IPTG (I) and aTc (J) in liquid culture. Lines represent the average fluorescence and error bars represent the standard deviation of 3 technical replicates for at least 3 independent experiments (see Fig. 1).

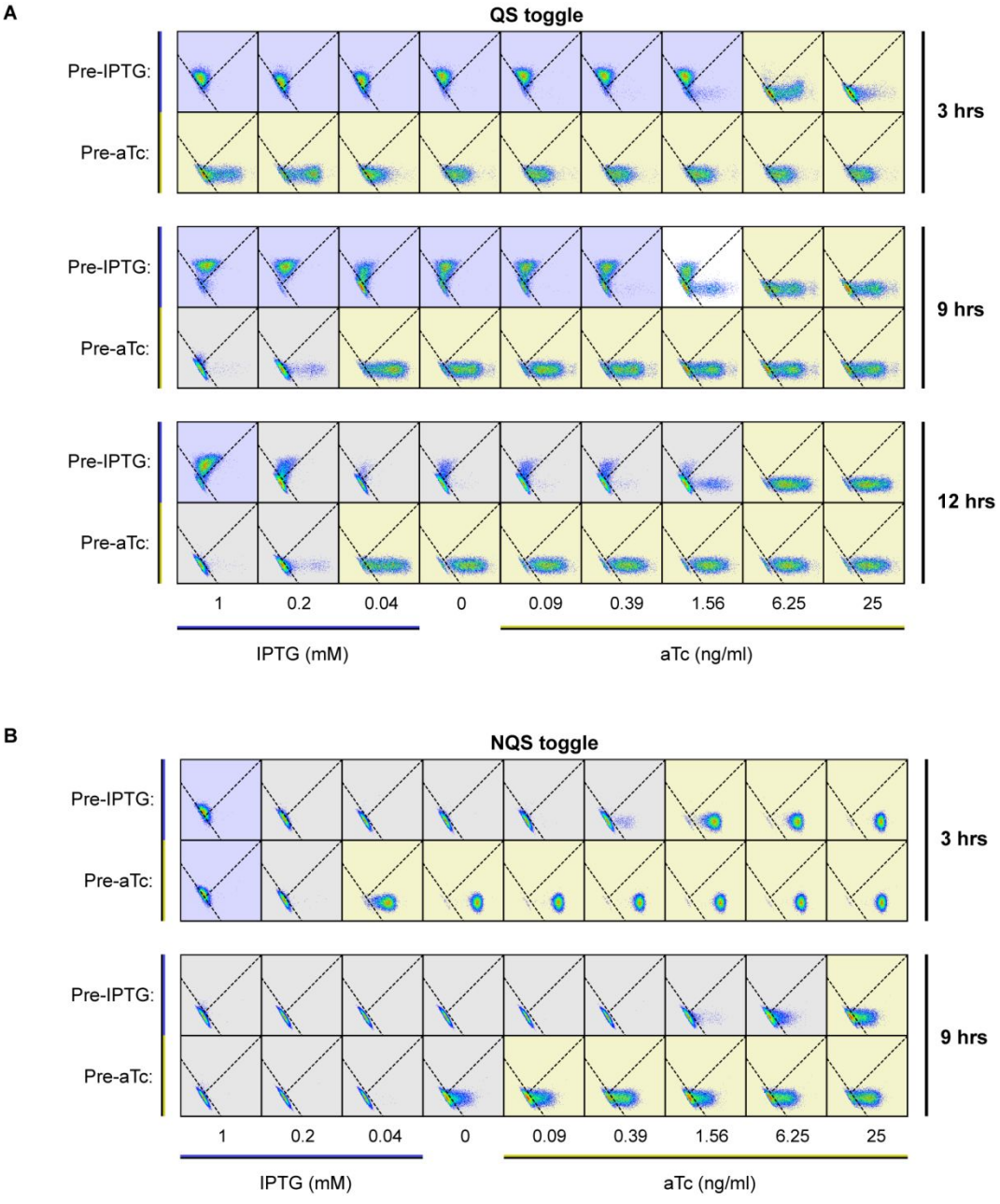

Figure S2: Individual behavior of QS and NQS toggle cells when treated with a single inducer for different duration of times. Flow cytometry data of QS and NQS toggle cells that were pre-induced with either IPTG or aTc. Each dot is a single cell classified within a gate. Gates were determined with single color and double negative controls.

Dashed lines in each plot represent the boundaries between the three distinct gates, which represent cellular states: CFP+ (top gate), YFP+ (bottom-right gate), and OFF (bottom-left gate). Background colors in each plot represent which state the majority of cells are in (>50%): blue color indicates mostly CFP+ cells, yellow plots are mostly YFP+, gray plots are mostly OFF, and white plots indicate cells that are present in multiple states (<50% each). **A)** QS toggle cells pre-treated with IPTG and aTc after growth for 3 (top), 9 (middle), and 12 hours (bottom). **B)** NQS toggle cells pre-treated with IPTG and aTc after growth for 3 (top) and 9 hours (bottom) (see Fig. 2).

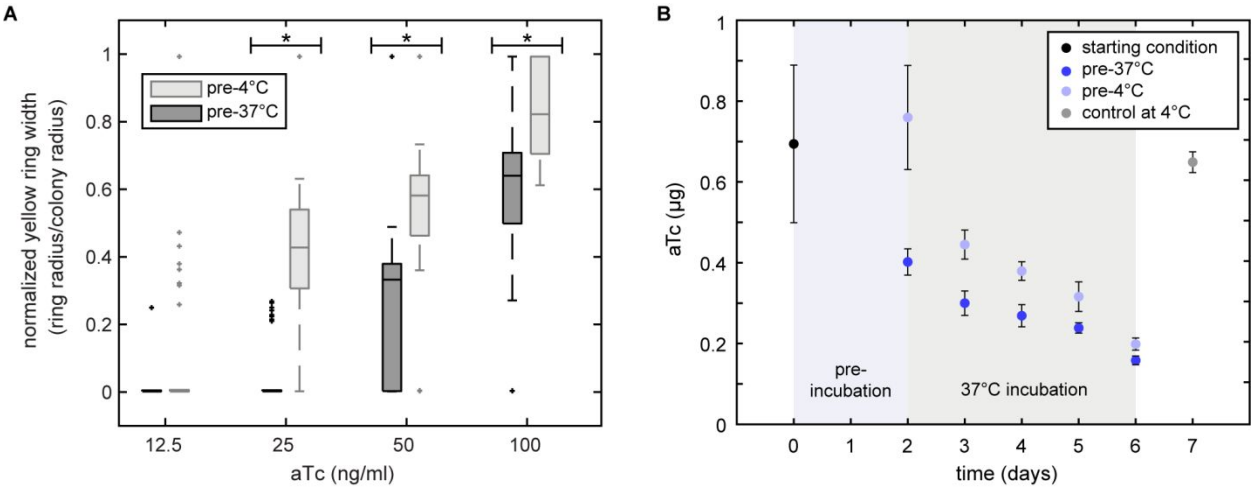

Figure S3: Incubation at 37°C causes aTc degradation. A) Yellow ring width measured from QS toggle colonies grown in aTc plates pre-incubated either at 4°C or 37°C for 48 hours prior to plating. Then, we plated and grew cells as shown in Fig. 3A. These values represent yellow ring widths from 76h post-plating. The 37°C plates showed a significant decrease in width in comparison to its 4°C counterparts, except at 12.5 ng/ml (*$p < 0.01$, Mann-Whitney non-parametric test). Data is from 5 independent experiments. Pre-4°C colonies are included in Fig. 3B. **B)** ATc quantification from LB agar extracts (in the absence of cells) with an HPLC. At time 0, aTc was quantified before any incubation. Samples were divided in two groups: pre-incubation for 48 hours at 37°C (bright blue), or 4°C (light blue) to recreate the experimental timeline in (A). On day 2, we incubated both groups at 37°C until day 6 to also recapitulate the experimental setup. As a control (gray), LB agar + aTc samples were kept at 4°C throughout the entire test and measured on day 7. Data represents mean ± standard deviation of 3 independent experiments (see Fig. 3).

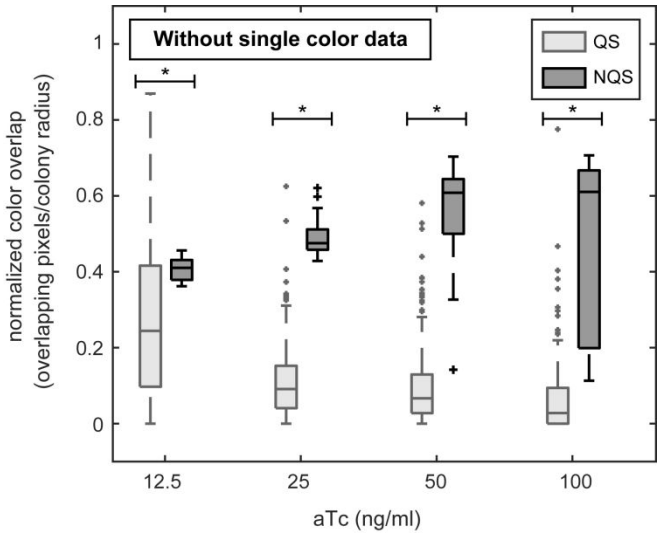

Figure S4: Quantification of pixel overlap for QS toggle (light gray) and NQS toggle (dark gray) colonies without single color data. We selected only colonies that have both colors present for at least 25% of the radius. We normalized the number of overlapping pixels by the colony radius (total pixels) ($p < 0.01$, Mann-Whitney non-parametric test). Data for each QS toggle test contains over 138 colonies from at least 11 independent experiments, while data for each NQS test contains at least 5 colonies from 2 independent experiments (see Fig. 4).

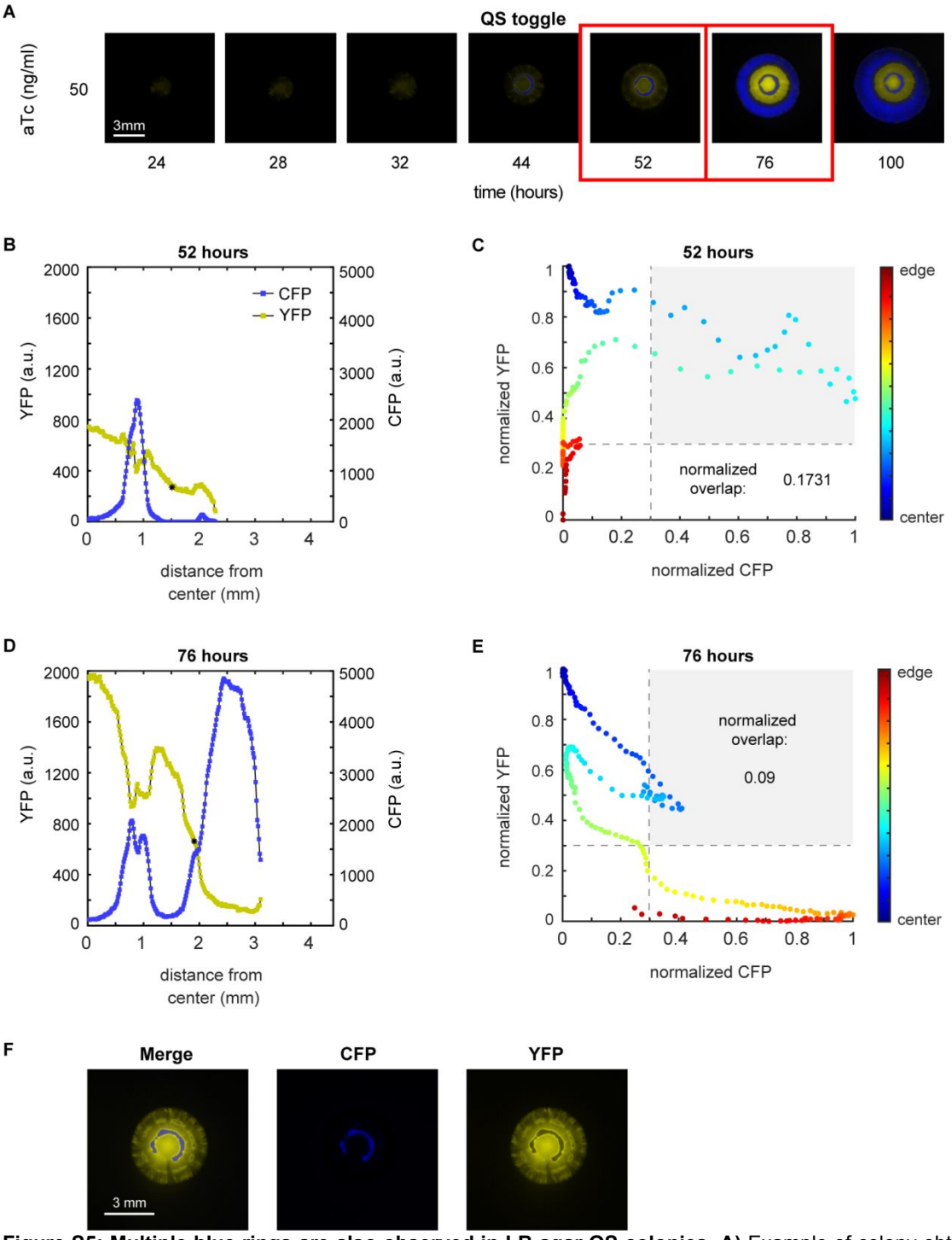

Figure S5: Multiple blue rings are also observed in LB agar QS colonies. A) Example of colony obtained from a 50 ng/ml aTc plate, over time. **B, C)** Fluorescence intensity cross-section at 52h and 76h, respectively, shown in (A). Curves are the average fluorescence between 4 radii of the same colony. **D, E)** We plotted each colony pixel from the images at 52h and 76h, respectively, for both normalized fluorescence values. We classified pixels as overlapping when both normalized fluorescence values were above a threshold of 0.3 (inside the gray boxed region). Curves are the average fluorescence between 4 radii of the same colony. **F)** Example of imperfectly symmetrical internal blue rings from a different colony at 52 hours post-plating (see Fig. 7).

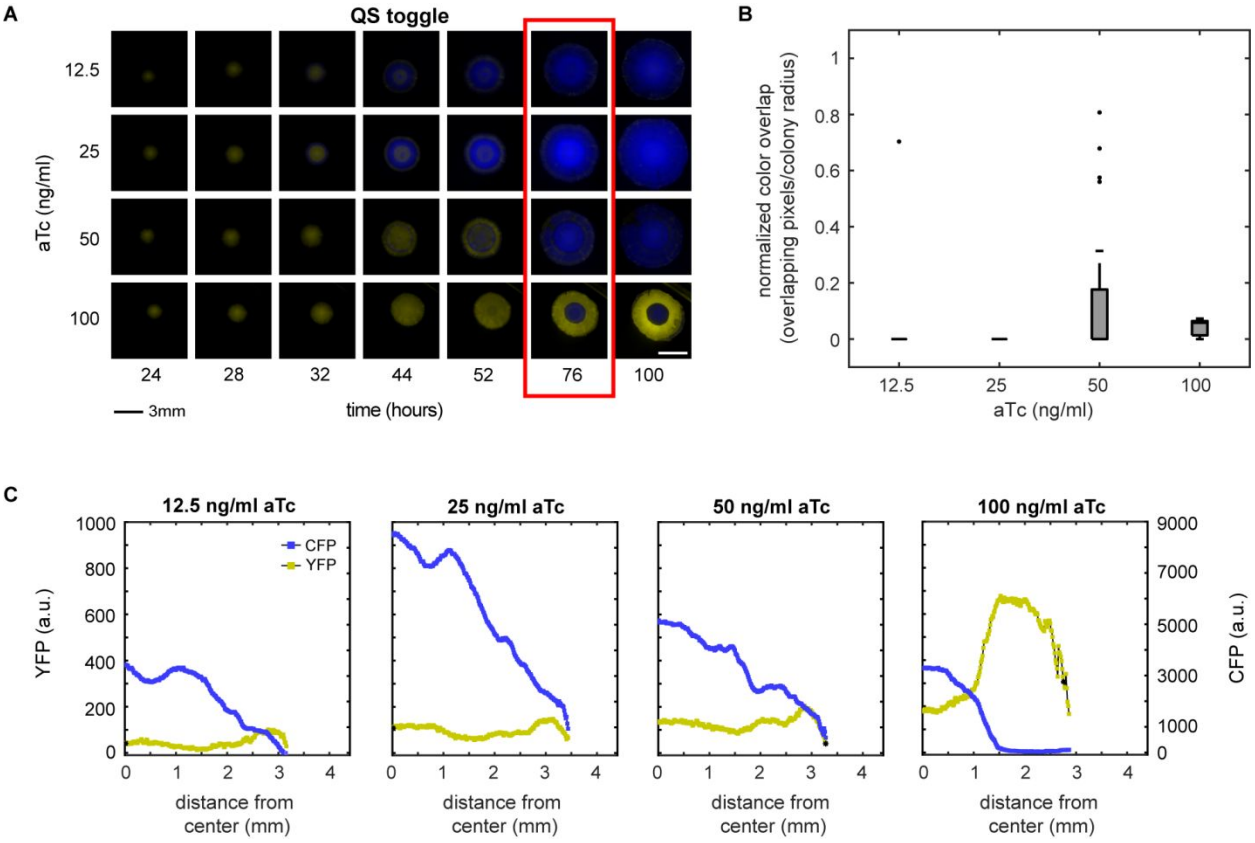

Figure S6: Expanding QS colonies in solid EZ rich defined medium. A) Colonies obtained from plates with different aTc concentrations, over time. At 100 ng/ml aTc, colonies remained all yellow or with blue center or internal ring fragments. **B)** We used the measurement of color overlap to quantify the spatial segregation of states per colony. We classified pixels as overlapping when both normalized fluorescence values were above a threshold of 0.3. Measurement of overlap was normalized by the colony radius (total number of pixels). Data is from 2 independent experiments. **C)** Fluorescence intensity cross-sectionals of colonies shown in (A). Curves are the average fluorescence between 4 radii of the same colony (see Fig. 7).

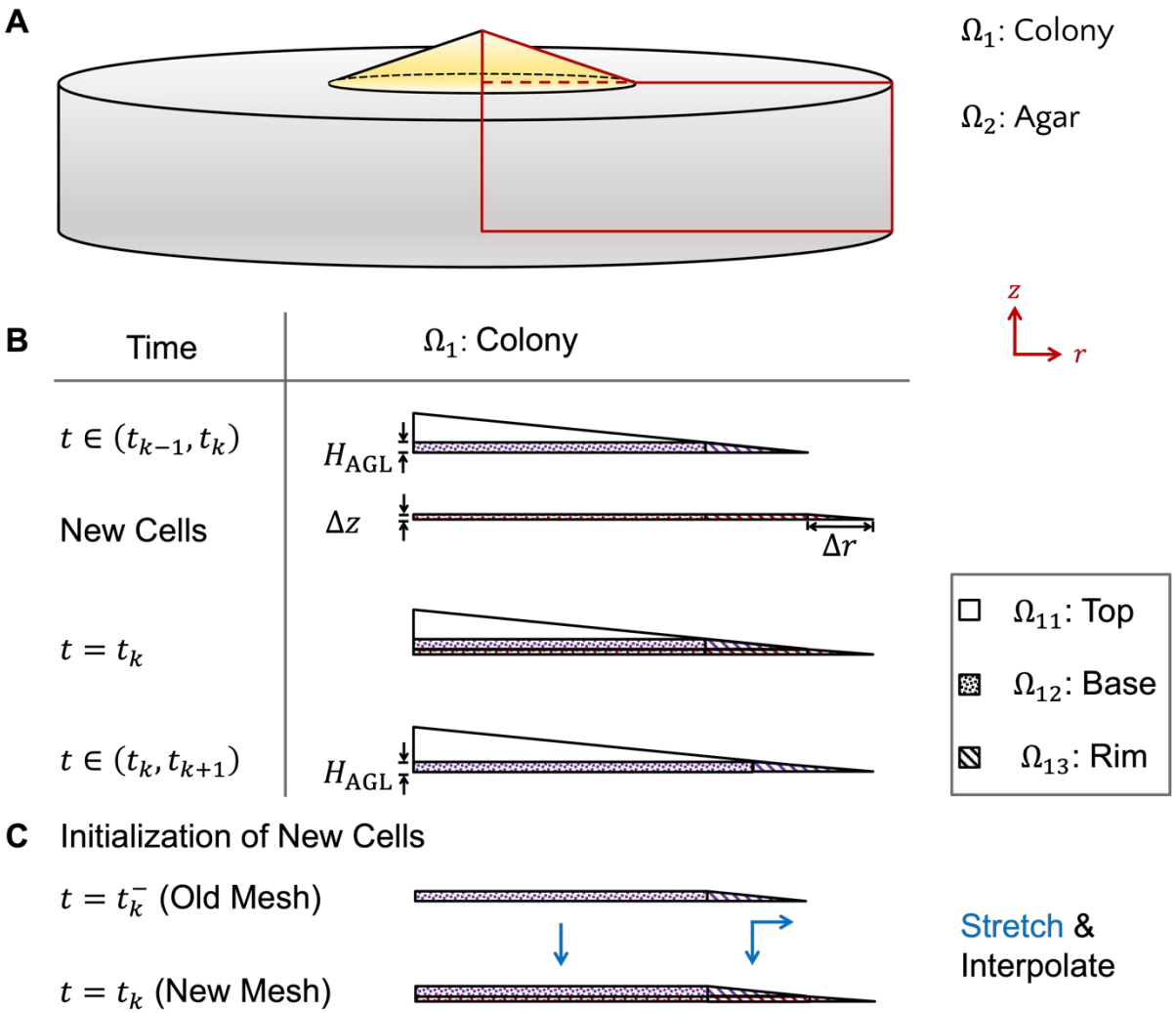

Figure S7: Schematics of the 3D domain and the discretization of the colony expansion used in numerical simulations. A) We assume a cone shaped growing colony sits on top of the cylindrical agar pad. The red curves outline a 2D slice from the 3D domain, in the radial (r) and height (z) direction. Assuming radial symmetry, which is consistent with experimental observations, we used this 2D slice as the domain for the model. The solid line represents the outer boundary ($\partial\Omega$) while the dashed line represents the inner boundary ($\partial\Omega^{\mathrm{in}}$). **B)** Growth is modeled by updating the colony's shape at even increments in time, Δt. At the end of each subinterval, the domain of the colony, Ω_1, is increased by adding a rectangle of height Δz and of width equal to that of the colony, and an adjoining right triangle of height Δz with base Δr. Here, we discretize time into intervals (t_{k-1}, t_k), with $t_k = k \cdot \Delta t$. **C)** After every increment of time, a new mesh is generated for the expanded colony. The new nodes at the Top and Rim region are initialized by interpolating the solution of the corresponding region from the stretched old mesh (see Fig. 5).

Table S1: List of genetic circuits and plasmids used in this work. All circuits were obtained by transforming three plasmids into CY027 strain (BW25113 derivative: Δ*araC* Δ*lacI* Δ*sdiA* +*cinR* +*rhlR*)[1]. In red are highlighted the -35/-10 promoters used for the relevant genes.

Circuit	Plasmid	Description	Origin	Resistance	Notes
QS toggle	pBM001	pCintet-dF-sfyfp-ssrA, pRhllac-dF-sfcfp-ssrA	pMB1+ROP	Kan	dF: strong promoters*[1,2]
	pBM002	pCintet-dF-lacI-ssrA, pRhllac-dF-tetR-ssrA, pAra-aiiA-ssrA	pSC101	Chlor	
	pBM003	pTet-fE-cinI-ssrA, pLac-fE-rhlI-ssrA, pCon-araC	p15A	Spec	fE: promoter with highest basal expression[1]
NQS toggle	pBM007	pTet-fE-sfyfp-ssrA, pLac-fE-sfcfp-ssrA	pMB1+ROP	Kan	
	pBM008	pTet-fE-lacI-ssrA, pLac-fE-tetR-ssrA	pSC101	Chlor	
	pBM009	Empty vector	p15A	Spec	To provide same resistance as QS toggle
Weaker blue state QS toggle	pBM010	pCintet-dF-sfyfp-ssrA, pRhllac-dE-sfcfp-ssrA	pMB1+ROP	Kan	dE: medium-strength promoters**[1,2]
	pBM011	pCintet-dF-lacI-ssrA, pRhllac-dE-tetR-ssrA, pAra-aiiA-ssrA	pSC101	Chlor	
	pBM003	Same from QS toggle	p15A	Spec	
Weaker QS toggle	pBM017	pCintet-dE-sfyfp-ssrA, pRhllac-dE-sfcfp-ssrA	pMB1+ROP	Kan	
	pBM018	pCintet-dE-lacI-ssrA, pRhllac-dE-tetR-ssrA, pAra-aiiA-ssrA	pSC101	Chlor	
	pBM003	Same from QS toggle	p15A	Spec	
Inverted QS toggle	pBM019	pRhltet-dE-sfyfp-ssrA, pCinlac-dE-sfcfp-ssrA	pMB1+ROP	Kan	
	pBM020	pRhltet-dE-lacI-ssrA, pCinlac-dE-tetR-ssrA, pAra-aiiA-ssrA	pSC101	Chlor	
	pBM021	pLac-fE-cinI-ssrA, pTet-fE-rhlI-ssrA, pCon-araC	p15A	Spec	

*These strong promoters are based on dF (-35/-10) promoters from Chen et al. (2018)[1], with one base pair change.

**Medium-strength promoters are based on dE (-35/-10) promoters from Chen et al. (2018)[1], with one base pair change. Medium-strength cin promoters also differ from strong cin promoters in the binding sequences. CinR binding sites are shown in Chen et al. (2015)[2], with strong named as pCin*, and medium-strength as pCin.

Table S2: List of parameters used in simulations unless otherwise mentioned in the text.

Type	Parameters	Description	Value	Units
NQS	a_1	LacI max. production rate	100	$\mathrm{nM} \cdot \mathrm{min}^{-1}$
	a_2	TetR max. production rate	250	$\mathrm{nM} \cdot \mathrm{min}^{-1}$
	u_0	aTc Concentration (low/medium/high)	15/30/60	nM
	k_+	aTc-TetR binding	0.06	$\mathrm{nM}^{-1} \cdot \mathrm{min}^{-1}$
	k_-	aTc-TetR unbinding	0.006	min^{-1}
QS	a_1	LacI max. production rate	110	$\mathrm{nM} \cdot \mathrm{min}^{-1}$
	a_2	TetR max. production rate	210	$\mathrm{nM} \cdot \mathrm{min}^{-1}$
	a_3	Effective C14 max. production rate	250	$\mathrm{nM} \cdot \mathrm{min}^{-1}$
	a_4	Effective C4 max. production rate	2000	$\mathrm{nM} \cdot \mathrm{min}^{-1}$
	u_0	aTc Concentration (low/medium/high)	24/30/36	nM
	k_+	aTc-TetR binding	0.006	$\mathrm{nM}^{-1} \cdot \mathrm{min}^{-1}$
	k_-	aTc-TetR unbinding	0.0006	min^{-1}
NQS/QS	γ_1	LacI degradation rate	$\ln 2/7$	min^{-1}
	γ_2	TetR degradation rate	$\ln 2/7$	min^{-1}
	γ_3	C14 degradation rate	$\ln 2/24$	h^{-1}
	γ_4	C4 degradation rate	$\ln 2/24$	h^{-1}
	γ_5	aTc degradation rate	$\ln 2/48$	min^{-1}
	θ_x	IC50 of LacI for $\mathrm{P_{Lac}}$	500	nM
	θ_y	IC50 of TetR for $\mathrm{P_{Tet}}$	500	nM
	θ_g	EC50 of C14 for $\mathrm{P_{Cin/Tet}}$	100	nM
	θ_h	EC50 of C4 for $\mathrm{P_{Rhl/Lac}}$	100	nM
	D_1^a	aTc diffusion in agar	400	$\mu\mathrm{m}^2 \cdot s^{-1}$
	D_1^c	aTc diffusion in colony	40	$\mu\mathrm{m}^2 \cdot s^{-1}$
	D_3^a	C14 diffusion in agar	10^2	$\mu\mathrm{m}^2 \cdot s^{-1}$
	D_3^c	C14 diffusion in colony	10	$\mu\mathrm{m}^2 \cdot s^{-1}$
	D_4^a	C4 diffusion in agar	10^3	$\mu\mathrm{m}^2 \cdot s^{-1}$
	D_4^c	C4 diffusion in colony	10^2	$\mu\mathrm{m}^2 \cdot s^{-1}$
	κ	Colony Aspect Ratio	1:10	-
	v_r	Radial growth rate	40	μm/h
	v_h	Vertical growth rate	4	μm/h
	H_{AGL}	Thickness of AGL	10	μm
	T	Time takes to grow H_{AGL}	2.5	h
	γ_d	dilution from linear growth	0.4	h^{-1}

Supporting movie legends

Movie S1: Patterning in the expanding QS toggle colony. Faster growth and balance of the QS signals at the rim leads to cells switching to the blue state. Bistability in the non-growing top leads to preservation of the yellow/blue states, as new cells are pushed out of the actively growing layer. This leads to a stable switching boundary in the radial direction. Top: aTc profile at different locations of the colony. Middle: 2D colormap of the LacI and TetR profile at different locations of the colony. Bottom three panels on left: normalized LacI and TetR concentration in the top-down view of the colony. Bottom right: Evolution of the effective promoter strength at the top and rim of the colony.

Movie S2: Patterning in the expanding NQS toggle colony. Once aTc drops below the hysteresis point, cells from the top start to switch to the blue state. Sequestration and degradation of aTc leads to the further spreading of the blue wave. Top: aTc profile at different locations of the colony. Middle: 2D colormap of the LacI and TetR profile at different locations of the colony. Bottom three panels on left: normalized LacI and TetR concentration in the top-down view of the colony. Bottom right: Evolution of the effective promoter strength at the top and rim of the colony.

References

(1) Chen, Y.; Ho, J. M. L.; Shis, D. L.; Gupta, C.; Long, J.; Wagner, D. S.; Ott, W.; Josić, K.; Bennett, M. R. Tuning the Dynamic Range of Bacterial Promoters Regulated by Ligand-Inducible Transcription Factors. *Nat Commun* **2018**, *9* (1), 64. https://doi.org/10.1038/s41467-017-02473-5.

(2) Chen, Y.; Kim, J. K.; Hirning, A. J.; Josić, K.; Bennett, M. R. Emergent Genetic Oscillations in a Synthetic Microbial Consortium. *Science (1979)* **2015**, *349* (6251), 986–989. https://doi.org/10.1126/science.aaa3794.